nature COMMUNICATIONS

ARTICLE

DOI: 10.1038/s41467-018-03218-8 OPEN

Large-area and bright pulsed electroluminescence in monolayer semiconductors

Der-Hsien Lien [1,2], Matin Amani [1,2], Sujay B. Desai [1,2], Geun Ho Ahn [1,2], Kevin Han [1], Jr-Hau He [3], Joel W. Ager III [2], Ming C. Wu [1] & Ali Javey [1,2]

Transition-metal dichalcogenide monolayers have naturally terminated surfaces and can exhibit a near-unity photoluminescence quantum yield in the presence of suitable defect passivation. To date, steady-state monolayer light-emitting devices suffer from Schottky contacts or require complex heterostructures. We demonstrate a transient-mode electroluminescent device based on transition-metal dichalcogenide monolayers (MoS_2, WS_2, $MoSe_2$, and WSe_2) to overcome these problems. Electroluminescence from this dopant-free two-terminal device is obtained by applying an AC voltage between the gate and the semiconductor. Notably, the electroluminescence intensity is weakly dependent on the Schottky barrier height or polarity of the contact. We fabricate a monolayer seven-segment display and achieve the first transparent and bright millimeter-scale light-emitting monolayer semiconductor device.

[1] Electrical Engineering and Computer Sciences, University of California, Berkeley, CA 94720, USA. [2] Materials Sciences Division, Lawrence Berkeley National Laboratory, Berkeley, CA 94720, USA. [3] Computer, Electrical and Mathematical Sciences and Engineering Division, King Abdullah University of Science & Technology, Thuwal 23955-6900, Saudi Arabia. Der-Hsien Lien, Matin Amani and Sujay B. Desai contributed equally to this work. Correspondence and requests for materials should be addressed to A.J. (email: ajavey@berkeley.edu)

Transition-metal dichalcogenides (TMDCs) such as WSe_2 and MoS_2 are semiconducting analogs of graphene, and are candidate materials for next-generation optoelectronic and electronic devices[1–5]. Their unique properties include naturally terminated surfaces at the monolayer limit (~0.7 nm), which when coupled with appropriate passivation of defect sites can result in near-unity photoluminescence (PL) quantum yield (QY)[3,6]. In addition, monolayer TMDCs display a myriad of attractive and unique physical properties including the lack of inversion symmetry, chiral light emission, and the ability to form heterostructures without the need for lattice matching[7–9]. Recent advances in the synthesis of high-quality TMDCs via chemical vapor deposition (CVD) demonstrate their potential for scalability[10,11]. The high PL QY and subnanometer thickness of TMDCs can be leveraged to develop large-area, transparent, and efficient light-emitting devices[3,6]. However, despite their exceptional material properties, a key challenge for TMDC light-emitting devices to date has been the formation of ohmic contacts to electrons and holes in the same device. Ohmic contacts in traditional light-emitting diodes (LEDs) are essential to minimize resistive losses and achieve high injection levels[12]. In previous works, steady-state electroluminescence (EL) was obtained in TMDCs using *p*–*n* junctions formed via electrostatic or chemical doping[13–15]. More recently, EL from complex quantum well heterostructures utilizing graphene with hexagonal boron-nitride tunnel barriers has been demonstrated[16,17]. However, the lack of suitable bipolar ohmic contacts remains to be a significant issue, ultimately limiting the performance of TMDC light-emitting devices[1].

Inspired by the first EL device, the light-emitting-capacitor[18–21], we achieve efficient bipolar carrier injection and light emission in TMDCs via transient-mode operation using a single metal-semiconductor contact (source). In this two-terminal device, the source is grounded and an AC voltage is applied to the gate electrode. Alternating electron and hole populations are injected into the monolayer TMDC from the source contact. Notably, the carrier injection is weakly dependent on the Schottky barrier height (φ_B) (i.e., polarity of the contact) because of the large tunneling currents present at the source during the gate-voltage (V_g) transients. The transient-EL (t-EL) device achieves bright EL at high injection levels. We demonstrate a millimeter-scale device with bright EL (peak power of 193 μW cm^{-2}) from a ~0.7 nm thick monolayer in ambient room lighting. Finally, we show a large area device fabricated on a quartz substrate, which is transparent in the off-state by using indium tin oxide (ITO) electrodes.

Results

Operation and structure of the t-EL device. Figure 1a shows a schematic of the t-EL device, consisting of a monolayer TMDC on a heavily doped silicon substrate (gate) with a 50 nm thick SiO_2 layer as the gate oxide. The TMDC is contacted with one metal electrode (source), and a bipolar square wave is applied between the gate and source. As shown in Fig. 1b, EL is only observed near the source contacts and the emission region laterally extends from the contact edge by ~3 μm (Supplementary Fig. 1). We fabricated devices based on four of the most heavily studied monolayer TMDCs by employing this generic device structure, specifically: WS_2, MoS_2, WSe_2, and $MoSe_2$[22,23]. All four of the studied materials show EL, with the spectral emission shape closely matching their respective PL (Fig. 1c).

Carrier injection and light-emission mechanism. We performed time-resolved EL (TREL) measurements to understand the dynamic performance and the mechanism of light emission in the t-EL device. The measured TREL from a WSe_2 device and the corresponding V_g square wave are shown in Fig. 2a and

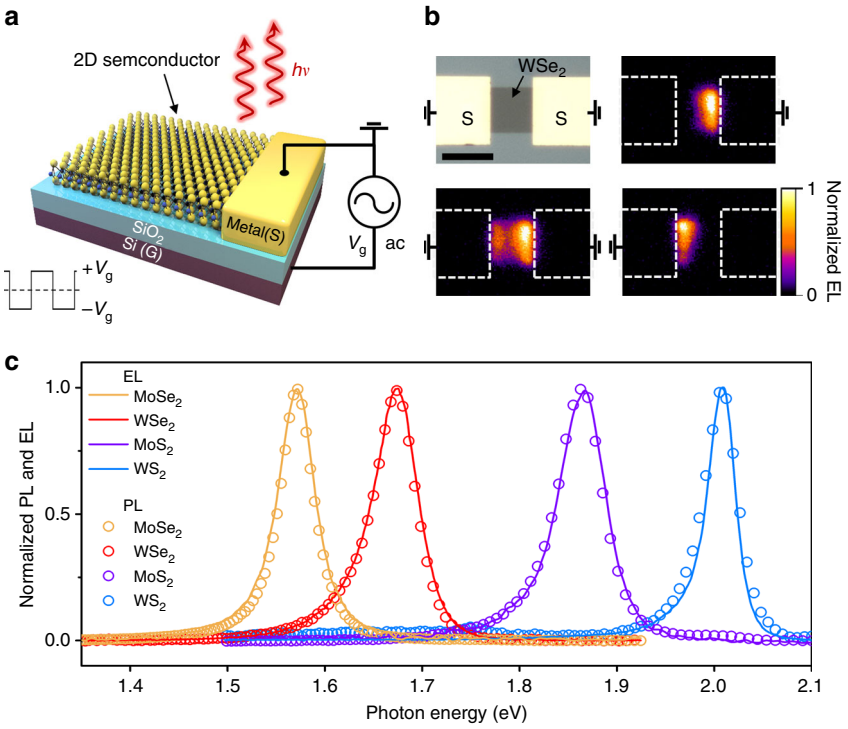

Fig. 1 Transient EL in TMDCs. **a** Schematic of the t-EL device. An AC voltage is applied between the gate and source electrodes and emission occurs near the source contact edge. **b** Optical and EL image of a WSe_2 device, showing that emission is only observed near the grounded source contacts. Scale bar is 10 μm. **c** EL and PL spectra measured for $MoSe_2$, WSe_2, MoS_2, and WS_2 monolayer devices

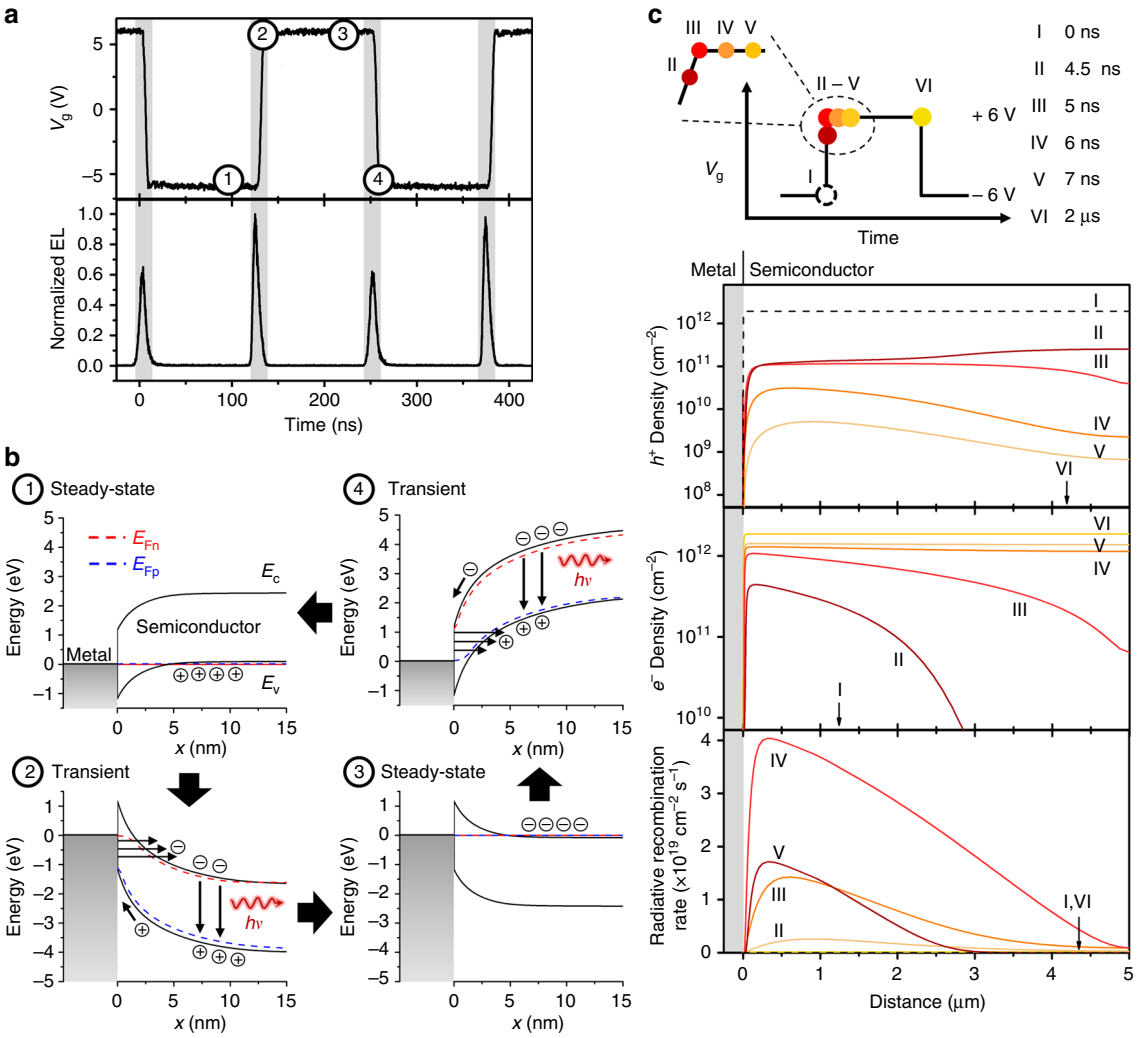

Fig. 2 Operation mechanism. **a** Time-resolved electroluminescence and the corresponding V_g, showing that EL occurs at the V_g transients (time points 2 and 4). **b** Band diagrams at different times during the operation cycle, corresponding to **a**. E_{Fn} and E_{Fp} indicate the quasi-Fermi levels for electrons and holes, respectively. **c** V_g pulse applied to the simulated device and the corresponding electron/hole density and radiative recombination rate. Simulations were performed for material parameters corresponding to WSe_2 using a 50 nm thick gate oxide and $V_g = \pm 6$ V (simulated band diagrams are also shown in Supplementary Figs. 5 and 6)

Supplementary Fig. 2 (the operation mechanism is also depicted in Supplementary Video 1). Pulsed EL is observed at each V_g transition and has a full-width half-maximum of 8 ns. EL emission in the device increases linearly with frequency (f) as shown in Supplementary Fig. 3 and Supplementary Note 2, with no changes in spectral shape. Note that the EL is stable with an approximately ±25%) intensity variation over time (Supplementary Fig. 4). The emission mechanism can be elucidated from the sequence of energy band diagrams (simulated via Sentaurus TCAD) shown in Fig. 2b, Supplementary Figs. 5 and 6 as well as the carrier densities and radiative recombination rate shown in Fig. 2c. When V_g is held at −6 V, the hole density in the semiconductor is large and approaches its steady-state value (p_0~1.9×10^{12} cm^{-2}). When V_g is switched to +6 V, the field across the capacitive component of the device (i.e., SiO_2 gate dielectric) cannot change instantaneously. As a result, the applied voltage is dropped across the resistive parts of the device including the semiconductor and the source contact, but is dominated by the latter. The large voltage drop and the steep energy band bending at the Schottky contact lead to large transient tunneling currents. Injected electrons diffuse inward while holes exit the semiconductor through the contact or recombine with incoming electrons. Thus, the hole density shows a continuous decrease, whereas the electron density in the semiconductor increases until it reaches its steady-state value (n_0~1.9×10^{12} cm^{-2}). At steady state, the band bending in the semiconductor and at the contact decreases (Supplementary Figs. 5 and 6) and the tunneling currents subside. The excess electron and hole populations simultaneously present (large quasi-Fermi level splitting) during the AC transient result in pulsed light emission. Similarly, this mechanism can also explain the emission from the device during a −6 V to +6 V V_g transient. The large transient tunneling currents in the t-EL device allow for efficient modulation of the carrier densities in the semiconductor, surmounting the large Schottky barriers typically associated with non-ohmic contacts to TMDCs. Simulated transient currents are shown in Supplementary Fig. 7 and the various current components present are discussed in detail in the Supplementary Note 3.

Schottky barrier height and gate-voltage dependence. The impact of φ_B on transient carrier injection and light emission is further studied by fabricating WSe_2 devices with electrodes prepared by sputtering (ITO), thermal evaporation (Au, Ag, Ni,

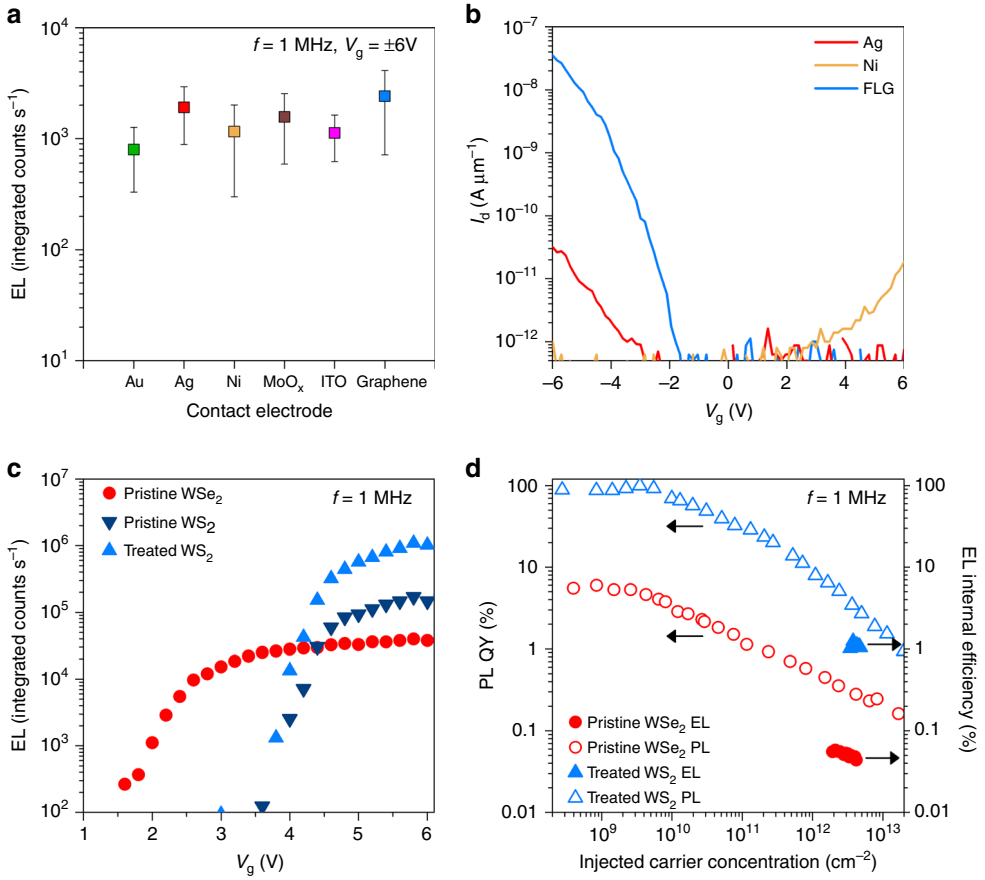

Fig. 3 Contact and voltage dependence. **a** EL from WSe_2 devices fabricated using various source contacts. Error bars indicate standard deviation of EL intensity measured from five or more different devices. **b** I_d–V_g characteristics of WSe_2 devices contacted by Ag, Ni, and few-layer graphene source electrodes. **c** Voltage dependence of EL for WSe_2 and WS_2 devices (WS_2 before and after superacid treatment). **d** PL QY and EL internal efficiency measured for a WSe_2 device and a superacid-treated WS_2 device as a function of injected carrier concentration

MoO_x), as well as transferred van der Waals few-layer graphene contacts. The different contacts result in ~3 orders of magnitude variation in the on-current when the device is configured as a transistor (Supplementary Fig. 8). However, the corresponding t-EL devices show a maximum variation in the integrated emission intensity of only ~4× as shown in Fig. 3a (error bars indicate standard deviation of EL intensity measured from five or more different devices). WSe_2 transistor characteristics for Ag, Ni, and graphene contracts are shown in Fig. 3b. Sentaurus TCAD simulations similarly show negligible difference in integrated EL for varying φ_B over the range of ohmic ($\varphi_B = 0.05$ eV) to mid-gap ($\varphi_B = E_g/2$) (Supplementary Fig. 9). The relative intensity of emission during the two V_g transients, however, does vary for devices with varying φ_B. As shown in the TREL of a hole selective contact device (Supplementary Fig. 10), the EL intensity at $+V_g$ to $-V_g$ transient is stronger than the other transient. This is consistent with simulation results (Supplementary Fig. 11) and discussed in the Supplementary Note 4. In addition to the effect of φ_B, we also studied the dependence of EL on varying V_g (Fig. 3c and Supplementary Fig. 12). EL is observed from the device when V_g is greater than the turn-on voltage (V_t), whose precise value is dependent on the bandgap (E_g) of the material and parasitic resistances in the device. We experimentally observe a higher V_t for WS_2 (4.1 V) as compared to WSe_2 (2.0 V) which is qualitatively consistent with the larger E_g of WS_2[24].

The efficiency in traditional light-emitting devices is defined as the number of emitted photons over the total current. However, for the t-EL device, transient current measurement is challenging due to device and measurement setup parasitic capacitances as well as the high slew rate (1.6 V ns^{-1}) of the V_g square wave. Given this limitation, we define EL internal efficiency (η_i) based on the total steady-state carrier concentration, which represents the maximum number of carriers that can undergo radiative recombination in a given V_g cycle. The efficiency is thus defined as: $\eta_i = \frac{\text{photons/cycle}}{(n_0+p_0)\times \text{area}}$ (Supplementary Equation 6). The sum of the steady-state concentrations, $(n_0 + p_0)$ is given by $C_g(2V_g\text{-}E_g\ \ q^{-1})q^{-1}$ (Supplementary Equation 7). Here, n_0 and p_0 are the steady-state electron and hole concentrations corresponding to a positive and negative V_g, respectively, C_g (69.1 nF cm^{-2} for 50 nm SiO_2 gate oxide) is the areal gate capacitance and q is the elementary charge. The analytical value of $n_0 + p_0$ closely matches that from simulations at sufficiently high V_g (Fig. 2c and Supplementary Fig. 13). η_i approaches 100% for the case where the PL QY is unity and all the steady-state carriers present in the device undergo recombination during a V_g transient. In practice, the PL QY may not be 100%, and only a fraction of the steady-state carriers will undergo recombination in the semiconductor, while the remainder exit through the contact due to the finite slew rate of the AC source. Further details on the efficiency calculation are provided in the Supplementary Note 6.

The WSe_2 t-EL device at $n_0 + p_0 = 2.1 \times 10^{12}$ cm^{-2} (calculated from Supplementary Equation 7 for $V_g = 3.2$ V and $E_g = 2.34$ eV) has an EL external efficiency (η_e) of 0.01% (Supplementary Fig. 14)[24]. The η_i of this device is extracted from η_e by considering the escape cone and optical interference from the Si substrate with a 50 nm SiO_2 layer[3,25]. Using this method, we calculate η_i of

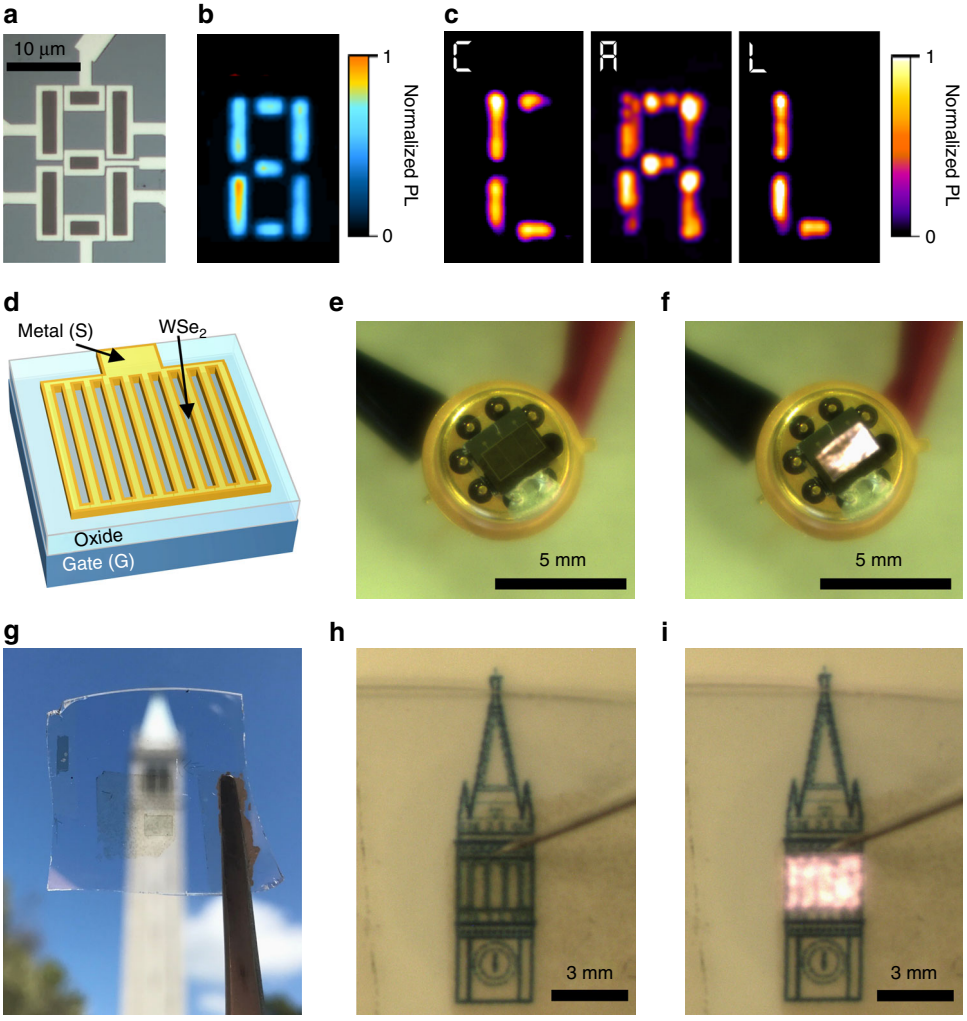

Fig. 4 Seven-segment display and millimeter-scale t-EL device. **a** Optical microscope image and **b** photoluminescence image of a seven-segment t-EL display. **c** Operation of the seven-segment display showing EL in the shape of C–A–L. **d** Schematic of a millimeter-scale device, showing the grid source electrode structure to increase active emission area. **e**, **f** Photograph of a packaged, 3 mm × 2 mm, device in the off **e** and on **f** state. **g** Photograph of a millimeter-scale transparent device. **h**, **i** Photograph of a large area (3 mm × 2 mm) transparent device in the off **h** and on **i** state

~0.06%. To contrast the performance of the t-EL device relative to the PL QY of the material, the steady-state and quasi-steady-state PL are measured using a continuous-wave and pulsed laser respectively (Fig. 3d, Supplementary Note 1, and Supplementary Fig. 15). The droop observed in PL QY at high injection levels has been previously attributed to biexcitonic recombination in two-dimensional (2D) semiconductors[3,6]. The calculated η_i for WSe_2~0.06% has an upper bound equal to the PL QY of the material (~0.3%) (Fig. 3d). The efficiency of the device can be improved by utilizing a material with a high PL QY. We fabricated WS_2 devices where the semiconductor surface is passivated using a non-oxidizing organic superacid: bis(trifluoromethane)sulfonimide, which has been shown to enhance the PL QY at low injection levels ($<10^9$ cm^{-2}) to >95%[3,6]. In this superacid-treated device, we obtain a peak η_e of ~0.27% at $n_0 + p_0$~3.8×10^{12} cm^{-2} (calculated from Supplementary Equation 7 for $V_g = 5.8$ V and $E_g = 2.88$ eV), corresponding to η_i~1.2% (the EL for this device before and after treatment are shown in Supplementary Fig. 16)[24]. We note that the η_i is still significantly limited by the PL QY droop at high injection levels (3.4%) (Fig. 3c and Supplementary Fig. 17). The effect of biexcitonic recombination on the PL QY is shown in Supplementary Fig. 18. This indicates that for pump levels in the range of 10^{12} cm^{-2}, WS_2 that has a C_{bx} of ~0.1 cm^2 s^{-1}, η_e can be improved to ~40% by sufficiently lowering C_{bx}. The next phase for improving the efficiency involves engineering the radiative lifetime and biexcitonic recombination rate by properly selecting the substrate and/or top coating. Similar efforts are made in III–V thin film devices, where the radiative recombination rate is highly dependent on the optical mode density and refractive index of the medium[26].

Seven-segment display and millimeter-scale t-EL device. To demonstrate the versatility of this transient injection mechanism, we fabricated the first display using TMDCs as the light-emitting material. A seven-segment display was fabricated using monolayer WSe_2 with Ni contacts. An optical image and the corresponding PL image of the display are shown in Fig. 4a, b, respectively. By grounding the source electrodes of individual elements in the display sequentially, we show that we can dynamically display the letters C–A–L. Furthermore, we show that the t-EL device can be readily scaled to millimeter dimensions by using large-area monolayer films of WSe_2 grown by CVD[11]. In order to maximize the light-emitting area, a Ni electrode is patterned in a grid structure with a line spacing of 8 µm (corresponding to ~2× of the emission FWHM, Supplementary Fig. 1). As a result, the EL from each contact edge fills the active area as

shown schematically in Fig. 4d. The final device was then packaged in a standard chip carrier. Figure 4e, f show photographs of a 3 mm × 2 mm device in operation under room lights. The average and peak output power of the device operating at $f = 400$ kHz, was measured directly using a power meter to be 0.62 μW cm^{-2} and 193 μW cm^{-2}, respectively. This shows that a monolayer semiconductor has the potential to be used in display and lighting applications. EL photographs of another device as well as the EL spectrum of the mm-scale device are shown in Supplementary Fig. 19. Finally, we demonstrate that the device can be made transparent as shown in Fig. 4g, with the corresponding transmission spectrum of the device shown in Supplementary Fig. 20. This device is fabricated on a fused quartz substrate, utilizing ITO as the gate and source electrodes and Al_2O_3 as the gate dielectric. Photographs of a transparent device in the off- and on-state are shown in Fig. 4h, i, respectively. Videos showing operation of both the transparent and opaque millimeter-scale devices are available in the Supplementary Information (Supplementary Videos 2 and 3, respectively).

In summary, we have demonstrated bright EL at high injection levels using transient-mode operation via a simple dopant-free device that does not require complex heterostructures to achieve light emission. EL from this device is weakly dependent on the Schottky barrier height or polarity. The transient-EL concept demonstrated in this work can be extended to large bandgap materials in the future, for which achieving ohmic contacts to both carrier types is particularly challenging. We show that this device structure can be scaled-up to obtain light emission on millimeter length scales. The ability to realize large-scale light emission from monolayer semiconductors opens numerous potential opportunities in the field of 2D materials and can lead to the realization of transparent displays. Our results also suggest that the main factors limiting the performance of the t-EL device is PL QY droop due to biexcitonic recombination. The device performance can be further improved through engineering of the optical medium[3,25]. Finally, unlike traditional LEDs, the exposed light-emitting surface of these devices also permits for the direct integration of plasmonic structures, nano-antennas, and photonic crystals, which could allow for the fabrication of high-speed devices or the development of electrically pumped 2D lasers[27–29].

Methods

Device fabrication. Devices based on MoS_2 (SPI supplies), WS_2 (HQ graphene), and $MoSe_2$ (HQ graphene) were fabricated from monolayers mechanically exfoliated onto 50 nm SiO_2/Si p^{++} substrates. The WSe_2 monolayers used in this work were synthesized by CVD with conditions tuned to optimize the PL QY of the material. Growth methods are presented in the reference[11], with the following modifications to obtain large area films: the Se boat temperature was ramped up to 130 °C and the growth time was extended to 42 min. The typical PL QY of synthesized WSe_2 samples at low pump powers is in the range of 5–15%. CVD WSe_2 monolayers were subsequently transferred to the desired substrate. For large area devices, WSe_2 films were transferred using a technique reported in reference[30] either to Si/SiO_2 or fused quartz/ITO/Al_2O_3 substrates. For patterning micron-scale devices on Si/SiO_2, the 2D material was first etched using XeF_2, while micron-scale devices on fused quartz/ITO/Al_2O_3 were etched using O_2/CF_4 plasma. Metal electrodes were subsequently deposited by thermal evaporation or sputtering. For graphene contacted devices, graphene flakes (three to five layers thick) were etched and subsequently placed on the TMDC using a previously reported dry transfer technique[9]. Due to the low PL QY of as-exfoliated MoS_2, devices were prepared using 40 nm thick Au contacts and subsequently were chemically treated using an organic superacid[3] to enhance the PL QY prior to EL measurements. All patterning was performed using electron-beam lithography with either poly (methyl methacrylate) (PMMA) or methyl methacrylate/PMMA as the resist. In the case of devices fabricated on quartz substrates, a 10 nm Au film was thermally evaporated on the PMMA and etched post e-beam lithography using KI/I_2 etchant. For the case of superacid-treated WS_2 devices shown in this work, few-layer graphene contacts were used. This was done in order to eliminate process-induced degradation of the 2D layer, which predominantly occurs during e-beam lithography.

Electrical and optical characterization. Electroluminescent devices were pumped using a bipolar square wave from an Agilent 33522A arbitrary waveform generator applied to the gate electrode, while the source contact was grounded. The PL and EL data presented in this work was measured using a custom built micro-PL instrument described in detail in reference[3] (Supplementary Methods). To measure PL, either a 514.5 nm Ar^+ laser or a monochromated 514 nm line from a pulsed supercontinuum laser was used as the excitation source. PL and EL were collected using either a 50× ultra-long working distance or a ×10 objective lens. The PL signal was passed through a 550 nm dielectric longpass filter to block the excitation light. Both PL and EL were dispersed by a spectrometer with a 340 mm focal length and 150 groove per mm grating, and detected using a Si charge-coupled device (CCD) (Andor iDus BEX2-DD). Prior to each measurement, the CCD background was obtained and subsequently subtracted from the PL/EL acquisition. Time-resolved EL measurements were collected using a time-correlated single-photon counting (TCSPC) module. The signal was detected with a low dark count avalanche photodiode operating in single-photon counting mode (IDQuantique). The timing for the TCSPC was determined using pulses generated with the same phase/frequency as the square wave applied to the gate of the device. PL and EL imaging were performed in a fluorescence microscopy setup using a 470 nm LED as the excitation source and a CCD detector (Andor Luca) to acquire images. For EL imaging, the illumination source was turned off. Macroscopic photographs and videos of EL were taken using a CMOS camera with a telephoto lens; images are single exposures taken in ambient room lighting. Note that for the macroscopic EL photographs, the cold filter was removed from the camera. All measurements reported in this paper are taken at room temperature, in an ambient lab environment, with no device encapsulation. Transistor I_d–V_g characteristics as well as C–f measurements of the gate oxide (Supplementary Fig. S21 and Supplementary Note 5) were taken using an Agilent B1500A semiconductor parameter analyzer.

Device simulations. Simulations were performed in Sentaurus TCAD, where the device structure consists of a monolayer of WSe_2, with the following material parameters used: $E_g = 2.34$ eV, $\varepsilon = 4\varepsilon_0$, $\mu_n = \mu_p = 100$ cm^2 V^{-1} per s, $\tau_{n,SRH} = \tau_{p,SRH} = 2.5$ ns, $m_e^* = m_h^* = 0.345\, m_0$, and a SiO_2 gate oxide thickness of 50 nm. A non-local tunneling model accounts for the dependence of tunneling currents at the metal-semiconductor contact. Simulation snapshots record the transient device characteristics, recombination rates, and carrier densities, at several different instances, immediately before, during and after a V_g pulse edge. The slew rate of the gate-voltage pulse used in the transient simulations is 2.4 V per ns. For simulations shown in Fig. 2, Supplementary Figs. 5, 6, and 13 ambipolar contacts ($\varphi_{Bn} = \varphi_{Bp} = E_g/2$) were used. The recombination models employed here are based on free carriers and material properties for GaAs were used for all parameters not specified above; however, the simulation adequately captures the physics of device operation and light emission qualitatively. For accurate quantitative analysis of this device, first-principle calculations and inclusion of the exciton physics of 2D materials are needed.

Data availability. The data that support the findings of this study are available from the corresponding author upon request.

Received: 2 November 2017 Accepted: 29 January 2018
Published online: 26 March 2018

References

1. Xia, F., Wang, H., Xiao, D., Dubey, M. & Ramasubramaniam, A. Two-dimensional material nanophotonics. *Nat. Photon.* **8**, 899–907 (2014).
2. Mak, K. F., Lee, C., Hone, J., Shan, J. & Heinz, T. F. Atomically thin MoS_2: a new direct-gap semiconductor. *Phys. Rev. Lett.* **105**, 136805 (2010).
3. Amani, M. et al. Near-unity photoluminescence quantum yield in MoS_2. *Science* **350**, 1065–1068 (2015).
4. Radisavljevic, B., Radenovic, A., Brivio, J., Giacometti, V. & Kis, A. Single-layer MoS_2 transistors. *Nat. Nanotechnol.* **6**, 147–150 (2011).
5. Desai, S. B. et al. MoS_2 transistors with 1-nanometer gate lengths. *Science* **354**, 99–101 (2016).
6. Amani, M. et al. Recombination kinetics and effects of superacid treatment in sulfur- and selenium-based transition metal dichalcogenides. *Nano Lett.* **16**, 2786–2791 (2016).
7. Wu, W. et al. Piezoelectricity of single-atomic-layer MoS_2 for energy conversion and piezotronics. *Nature* **514**, 470–474 (2014).
8. Zhang, Y. J., Oka, T., Suzuki, R., Ye, J. T. & Iwasa, Y. Electrically switchable chiral light-emitting transistor. *Science* **344**, 725–728 (2014).
9. Fang, H. et al. Strong interlayer coupling in van der Waals heterostructures built from single-layer chalcogenides. *Proc. Natl Acad. Sci. USA* **111**, 6198–6202 (2014).
10. Kang, K. et al. High-mobility three-atom-thick semiconducting films with wafer-scale homogeneity. *Nature* **520**, 656–660 (2015).
11. Ahn, G. H. et al. Strain-engineered growth of two-dimensional materials. *Nat. Commun.* **8**, 608 (2017).

12. Nakamura, S., Senoh, M. S. & Mukai, T. High-power InGaN/GaN double-heterostructure violet light emitting diodes. *Appl. Phys. Lett.* **62**, 2390–2392 (1993).
13. Ross, J. S. et al. Electrically tunable excitonic light-emitting diodes based on monolayer WSe_2 p-n junctions. *Nat. Nanotechnol.* **9**, 268–272 (2014).
14. Baugher, B. W. H., Churchill, H. O. H., Yang, Y. & Jarillo-Herrero, P. Optoelectronic devices based on electrically tunable p-n diodes in a monolayer dichalcogenide. *Nat. Nano* **9**, 262–267 (2014).
15. Pospischil, A., Furchi, M. M. & Mueller, T. Solar-energy conversion and light emission in an atomic monolayer p-n diode. *Nat. Nanotechnol.* **9**, 257–261 (2014).
16. Withers, F. et al. Light-emitting diodes by band-structure engineering in van der Waals heterostructures. *Nat. Mater.* **14**, 301–306 (2015).
17. Withers, F. et al. WSe_2 light-emitting tunneling transistors with enhanced brightness at room temperature. *Nano Lett.* **15**, 8223–8228 (2015).
18. Butler, K. H., Jerome, C. W. & Waymouth, J. F. The electroluminescent lamp: a new light source. *Electr. Eng.* **73**, 524–528 (1954).
19. Wood, V. et al. Electroluminescence from nanoscale materials via field-driven ionization. *Nano Lett.* **11**, 2927–2932 (2011).
20. Cho, S. H. et al. High performance AC electroluminescence from colloidal quantum dot hybrids. *Adv. Mater.* **24**, 4540–4546 (2012).
21. Xu, J., Carroll, D. L., Smith, G. M., Dun, C. & Cui, Y. Achieving high performance in AC-field driven organic light sources. *Sci. Rep.* **6**, 24116 (2016).
22. Gutierrez, H. R. et al. Extraordinary room-temperature photoluminescence in triangular WS_2 monolayers. **13**, 3447–3454 (2013).
23. Tonndorf, P. et al. Photoluminescence emission and Raman response of monolayer MoS_2, $MoSe_2$, and WSe_2. *Opt. Express* **21**, 4908–4916 (2013).
24. Ramasubramaniam, A. Large excitonic effects in monolayers of molybdenum and tungsten dichalcogenides. *Phys. Rev. B* **86**, 115409 (2012).
25. Lien, D.-H. et al. Engineering light outcoupling in 2D materials. *Nano Lett.* **15**, 1356–1361 (2015).
26. Yablonovitch, E., Gmitter, T. J. & Bhat, R. Inhibited and enhanced spontaneous emission from optically thin AlGaAs/GaAs double heterostructures. *Phys. Rev. Lett.* **61**, 2546–2549 (1988).
27. Ciraci, C. et al. Probing the ultimate limits of plasmonic enhancement. *Science* **337**, 1072–1074 (2012).
28. Eggleston, M. S., Messer, K., Zhang, L., Yablonovitch, E. & Wu, M. C. Optical antenna enhanced spontaneous emission. *Proc. Natl Acad. Sci. USA* **112**, 1704–1709 (2014).
29. Wu, S. et al. Monolayer semiconductor nanocavity lasers with ultralow thresholds. *Nature* **520**, 69–72 (2015).
30. Ma, D. et al. A universal etching-free transfer of MoS_2 films for applications in photodetectors. *Nano Res.* **8**, 3662–3672 (2015).

Acknowledgements

We thank A.B. Sachid for advice on device simulations. Device fabrication and characterization were funded by the National Science Foundation (NSF) under program number 1623038. Materials growth was supported by the U.S. Department of Energy, Office of Science, Office ofBasic Energy Sciences, Materials Sciences and Engineering Division under contract no.DE-AC02-05CH11231 within the Electronic Materials Program (KC1201). S.B.D. acknowledges the Lam Research Graduate Fellowship.

Author contributions

D.-H.L., M.A., and A.J. conceived the idea for the project and designed the experiments. D.-H.L. and M.A. performed optical measurements. M.A. and G.H.A. fabricated devices. G.H.A. performed the synthesis of WSe_2. S.B.D. performed device simulations. S.B.D. and K.H. performed analytical modeling. D.-H.L., M.A., S.B.D., and A.J. analyzed the data. M.A., D.-H.L., S.B.D., and A.J. wrote the manuscript. All authors discussed the results and commented on the manuscript.

Additional information

Supplementary Information accompanies this paper at https://doi.org/10.1038/s41467-018-03218-8.

Competing interests: The authors declare no competing financial interests.

Reprints and permission information is available online at http://npg.nature.com/reprintsandpermissions/

Publisher's note: Springer Nature remains neutral with regard to jurisdictional claims in published maps and institutional affiliations.

Open Access This article is licensed under a Creative Commons Attribution 4.0 International License, which permits use, sharing, adaptation, distribution and reproduction in any medium or format, as long as you give appropriate credit to the original author(s) and the source, provide a link to the Creative Commons license, and indicate if changes were made. The images or other third party material in this article are included in the article's Creative Commons license, unless indicated otherwise in a credit line to the material. If material is not included in the article's Creative Commons license and your intended use is not permitted by statutory regulation or exceeds the permitted use, you will need to obtain permission directly from the copyright holder. To view a copy of this license, visit http://creativecommons.org/licenses/by/4.0/.

© The Author(s) 2018

Supplementary Figures

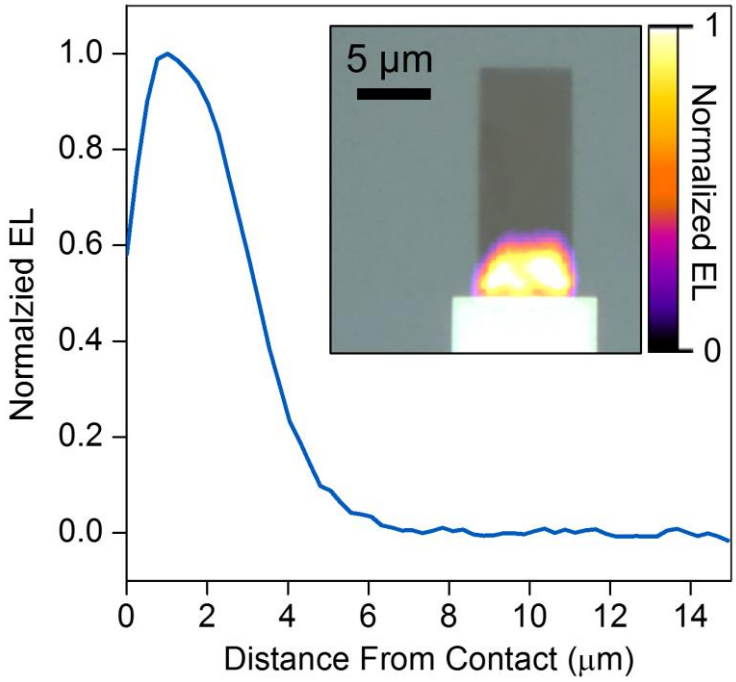

Supplementary Figure 1 | Spatial profile of EL. Spatial profile of EL intensity for a WSe_2 t-EL device fabricated with a single source contact. Inset shows superimposed optical and EL image. Measurement was taken with V_g = ± 9V at a frequency of 1 MHz. The EL peak is ~1 μm from the contact edge with a FWHM of ~3.3 μm; note that the experimental values are limited by the resolution of the optical system (~500 nm).

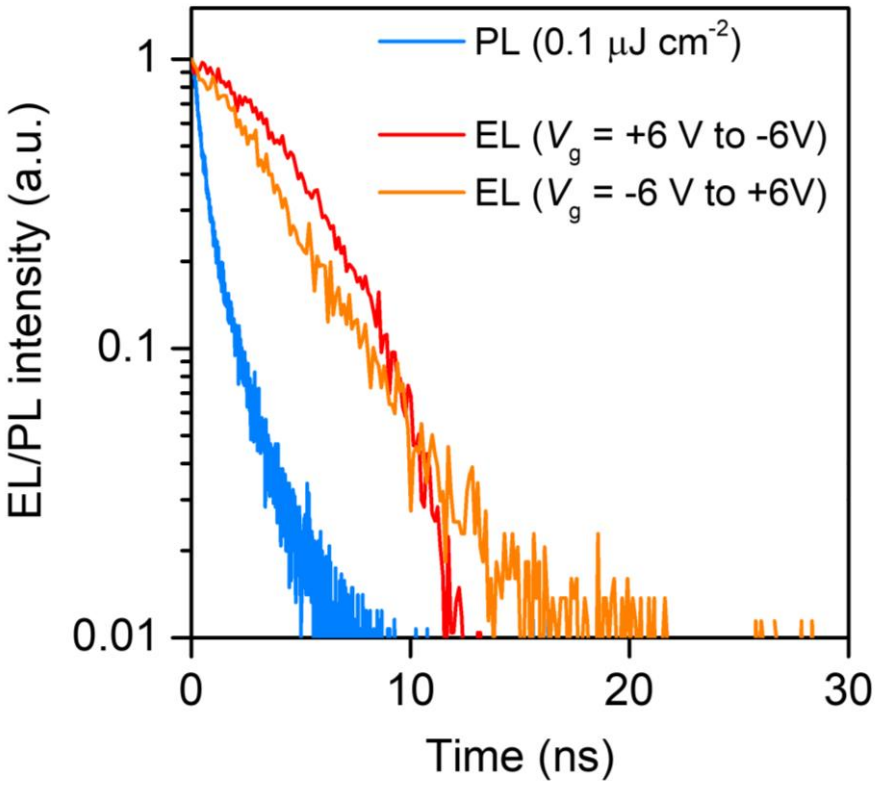

Supplementary Figure 2 | TRPL and TREL decay. Time resolved PL decay measured at an injection level of 0.1 μJ cm^{-2} and time resolved EL decay measured at gate transitions of V_g = +6 V to -6 V and V_g = -6 V to +6 V.

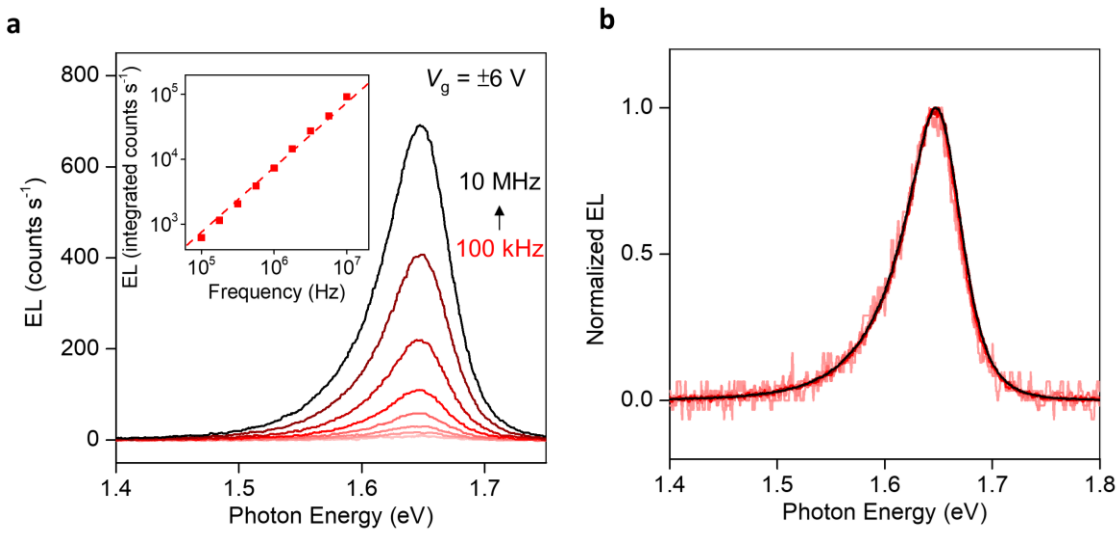

Supplementary Figure 3 | Frequency dependence. (a) EL spectra of a WSe_2 device operated at gate frequencies ranging from 100 kHz to 10 MHz. Inset shows integrated EL counts per cycle as a function of operating frequency. The superlinar increases EL versus frequency is attributed to time dependent variation in the device (Supplementary Fig. 4). **(b)** Normalized EL spectra of Supplementary Fig. 3a.

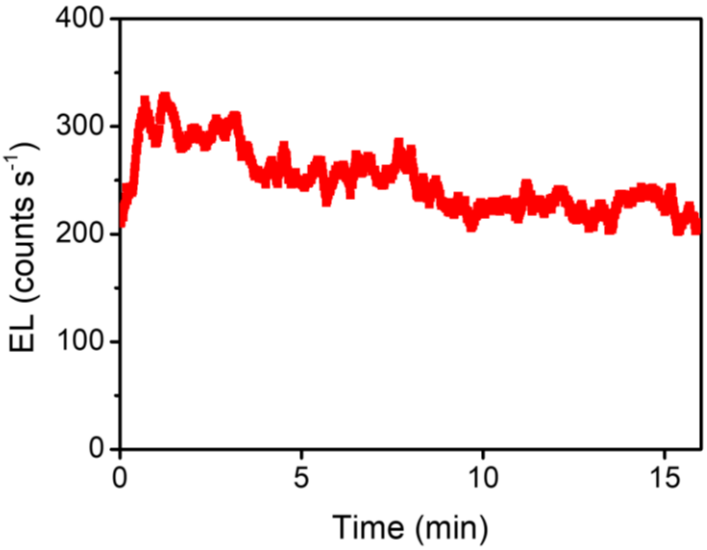

Supplementary Figure 4 | Device stability. EL counts measured for a WSe_2 device operated for fifteen minutes in ambient with no encapsulation. The device shows a maximum variation of 50% over the full operation time.

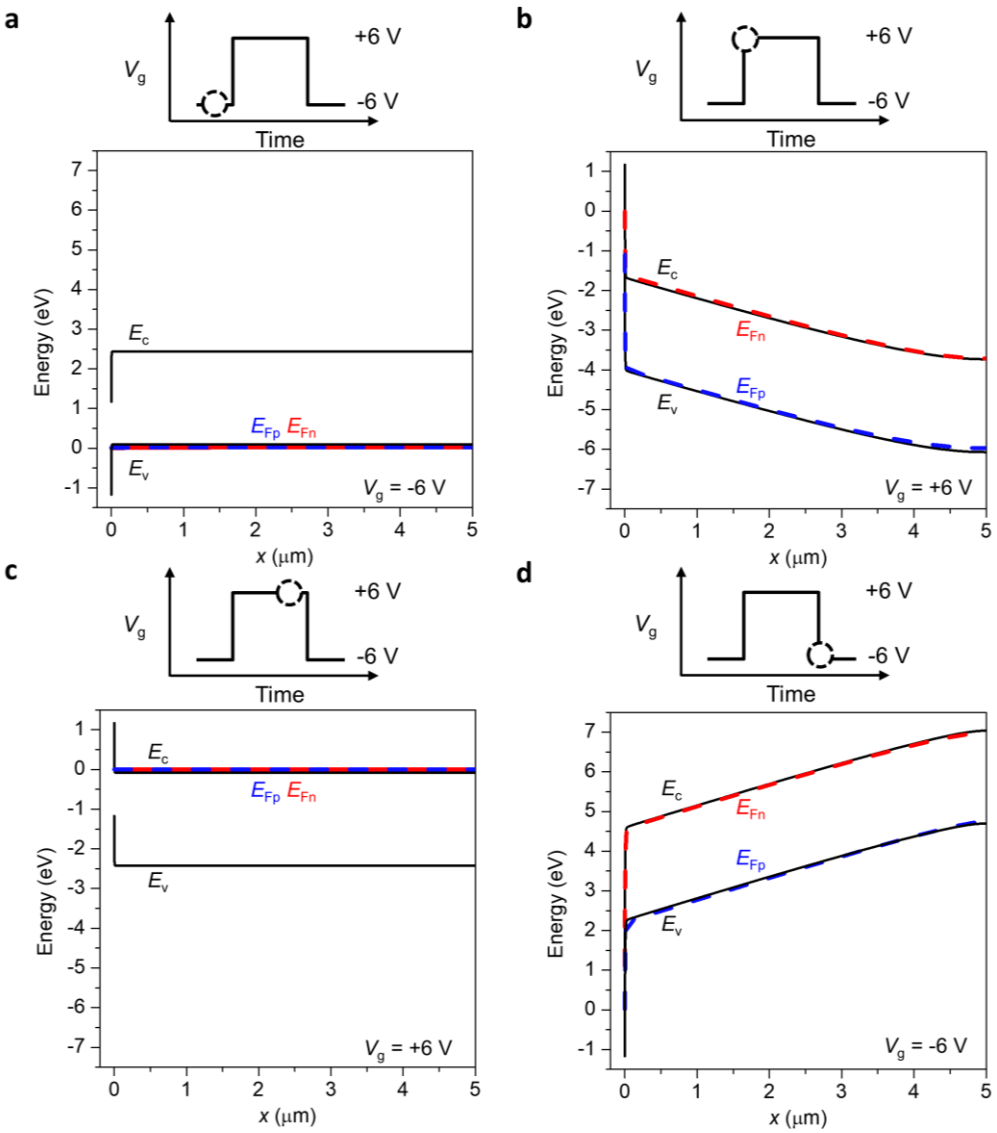

Supplementary Figure 5 | Simulated band diagrams. (a) Band diagram at V_g = -6 V, immediately before V_g transient. **(b)** Band diagram immediately after switching bias to V_g = +6 V. **(c)** Band diagram at V_g = +6 V, immediately before V_g transient. **(d)** Band diagram immediately after switching bias to V_g = -6 V. Simulations were performed for material parameters corresponding to WSe_2, further details are provided in the methods.

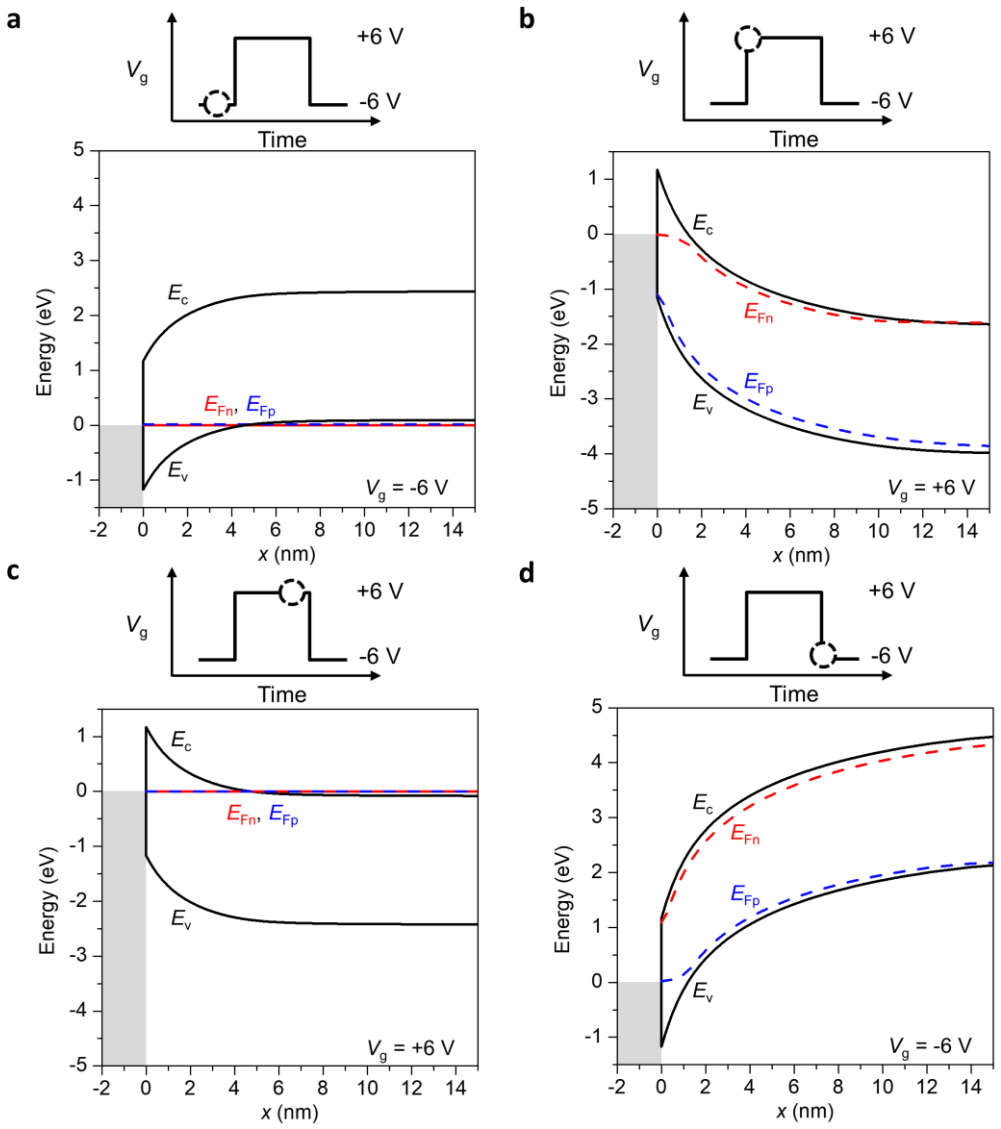

Supplementary Figure 6 | Simulated band diagrams near the contact edge. Data shown here is from Supplementary Fig. 5, expanded near the Schottky contact for clarity. **(a)** Band diagram at V_g = -6 V, immediately before V_g transient. **(b)** Band diagram immediately after switching bias to V_g = +6 V. **(c)** Band diagram at V_g = +6 V, immediately before V_g transient. **(d)** Band diagram immediately after switching bias to V_g = -6 V. Simulations were performed for material parameters corresponding to WSe_2, further details are provided in the methods.

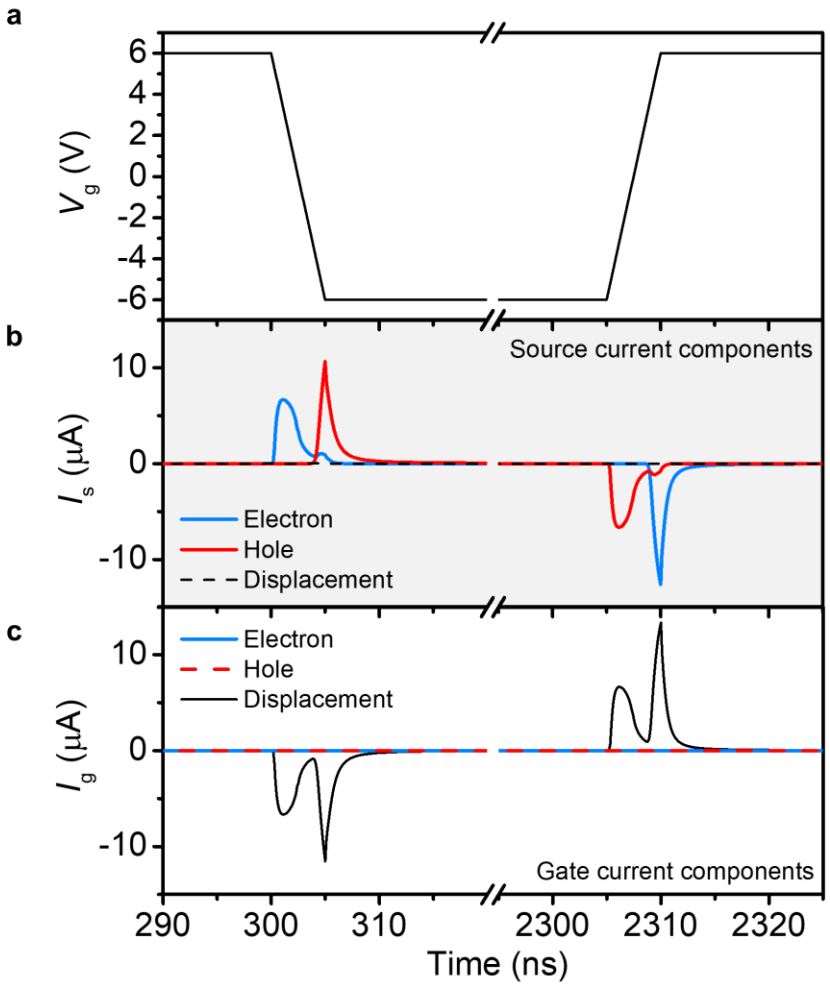

Supplementary Figure 7 | Transient current components. (a) V_g as a function of time. Corresponding source (I_s) and gate (I_g) currents are shown in **(b)** and **(c)**, respectively. I_s is dominated by electron and hole components, while the displacement current is relatively negligible. I_g is dominated by the displacement current. Simulations were performed for material parameters corresponding to WSe_2, further details are provided in the methods.

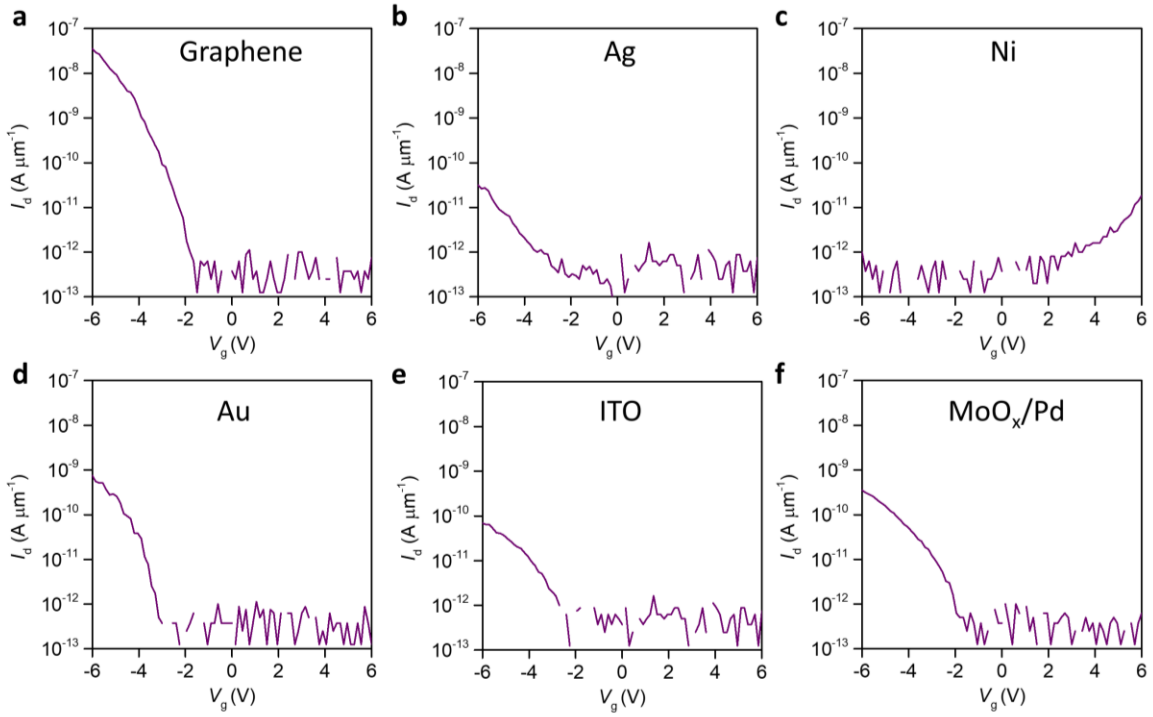

Supplementary Figure 8 | I_d-V_g characteristics of WSe_2 devices with various contacts. I_d-V_g characteristics of representative WSe_2 devices shown in Fig. 3a, fabricated with **(a)** transferred few-layer graphene (FLG) contacts, **(b)** thermally evaporated Ag, **(c)** thermally evaporated Ni, **(d)** thermally evaporated Au **(e)** sputtered ITO, and **(f)** thermally evaporated MoO_x/Pd[1]. $|V_{ds}|$ = 1 V for all cases.

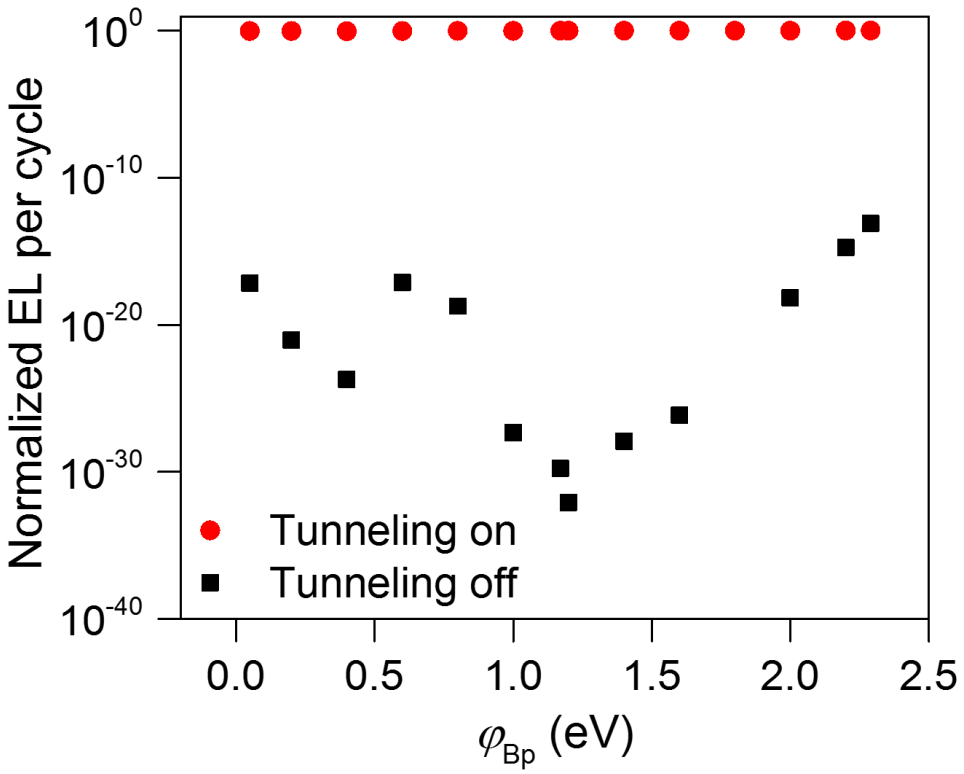

Supplementary Figure 9 | Dependence of EL on Schottky barrier height. Simulated EL integrated per gate cycle for a device where the Schottky barrier height is varied (note that $\varphi_{Bn} + \varphi_{Bp} = E_g$). Simulations were performed in the case where tunneling was allowed (red circles) and unaccounted for (black squares). Simulated EL shows negligible dependence on the Schottky barrier height when we account for the tunneling current. The integrated EL intensity for the case where the tunneling model is off is orders of magnitude lower and is dependent on the Schottky barrier height and several simulation parameters such as gate work function, which was assumed to be 5.1 eV. Simulations were performed for material parameters corresponding to WSe_2, further details are provided in the methods.

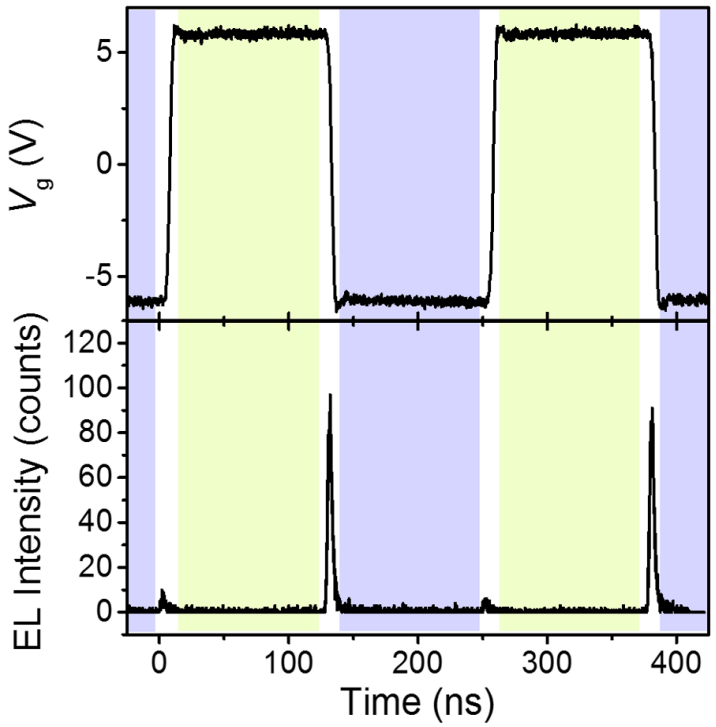

Supplementary Figure 10 | TREL of a WSe_2 device with unipolar MoO_x/Pd contacts. TREL measured for a WSe_2 device with unipolar MoO_x/Pd contacts, which show a large Schottky barrier to electrons and a low Schottky barrier to holes.

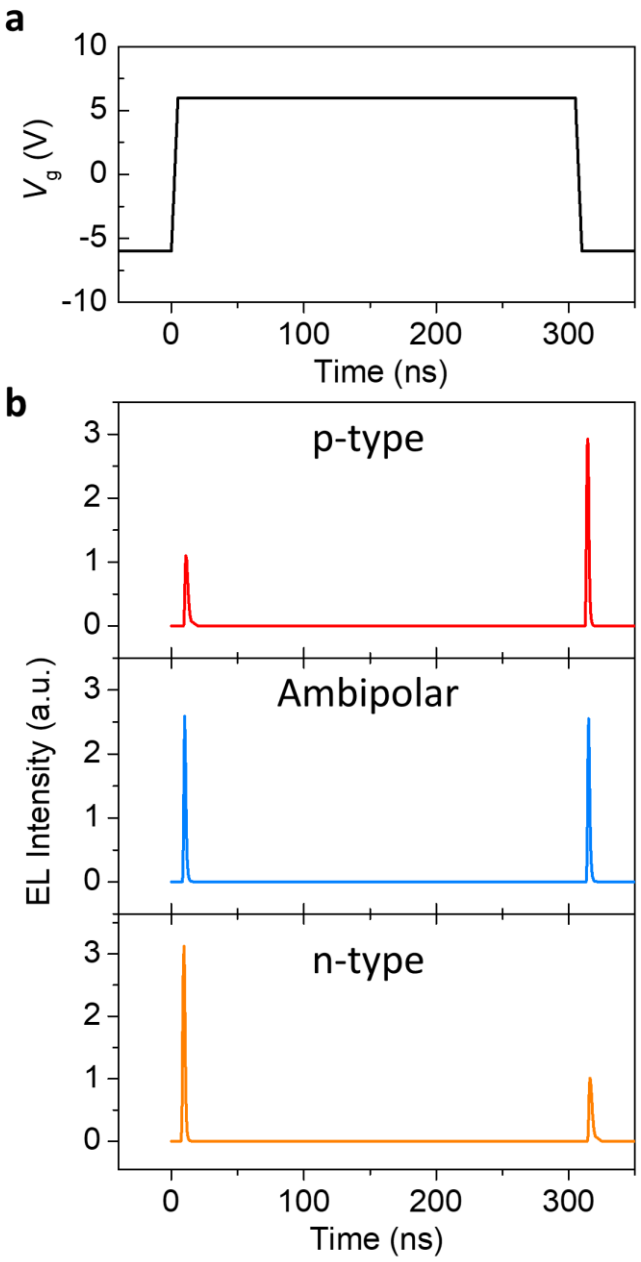

Supplementary Figure 11 | Simulated TREL for p-type, ambipolar and n-type devices. (a) Gate voltage as a function of time. **(b)** Simulated TREL for devices with varying Schottky barrier height; specifically, the cases of Fermi level pinning at conduction band (n-type), mid-gap (ambipolar) and valance band (p-type). Simulations were performed for material parameters corresponding to WSe_2, further details are provided in the methods.

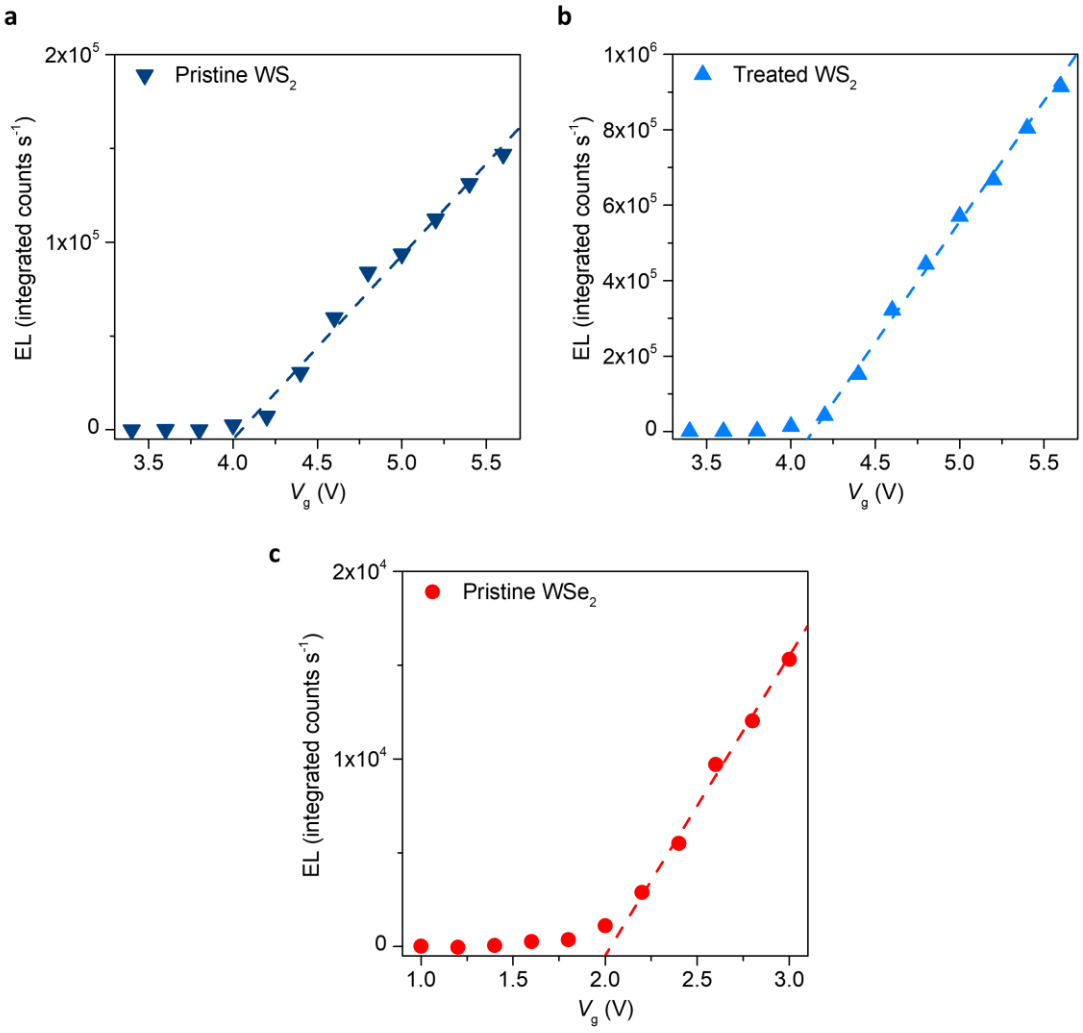

Supplementary Figure 12 | V_g dependence of EL characteristics. EL measured for a WS_2 device before **(a)**, and after superacid treatment **(b)**, as well as a WSe_2 device **(c)**, as a function of injected carrier concentration. Note that V_t for the WSe_2 and WS_2 devices are 2.0 V and 4.1 V, respectively.

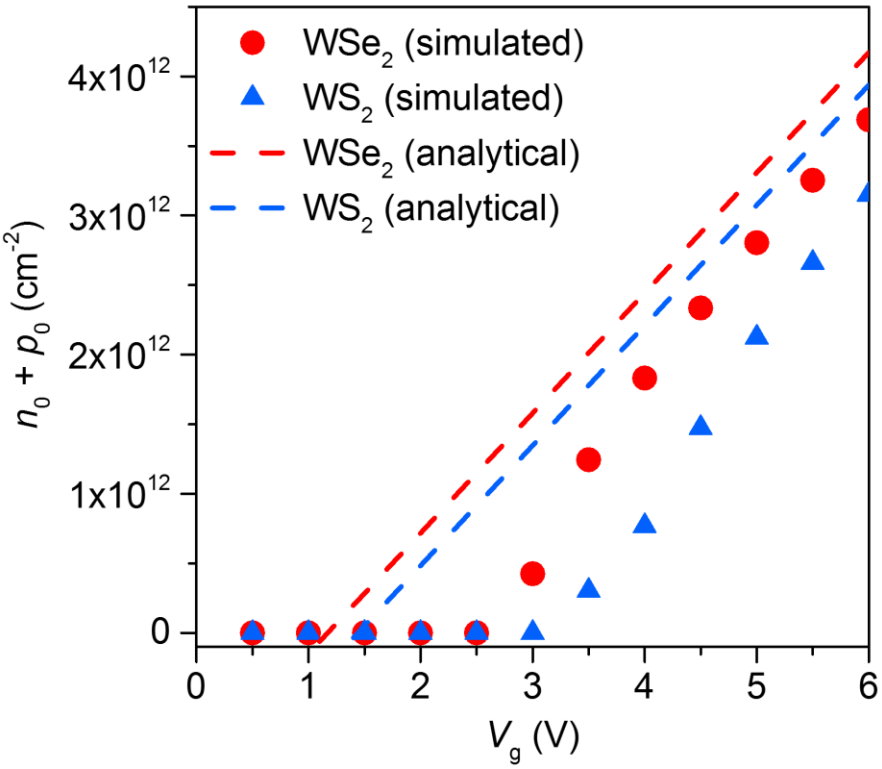

Supplementary Figure 13 | Total steady-state injected carrier concentration as a function of applied voltage. n_0+p_0 extracted from simulations and calculated using Supplementary Equation 4 for WSe_2 and WS_2 devices as a function of applied V_g. The injected carrier concentration at low V_g is overestimated by Supplementary Equation 4 because it does not account for the voltage dropped across the length of the semiconductor during a V_g transient. E_g values used for the simulations and analytical calculations are 2.34 eV and 2.88 eV for WSe_2 and WS_2 respectively[2].

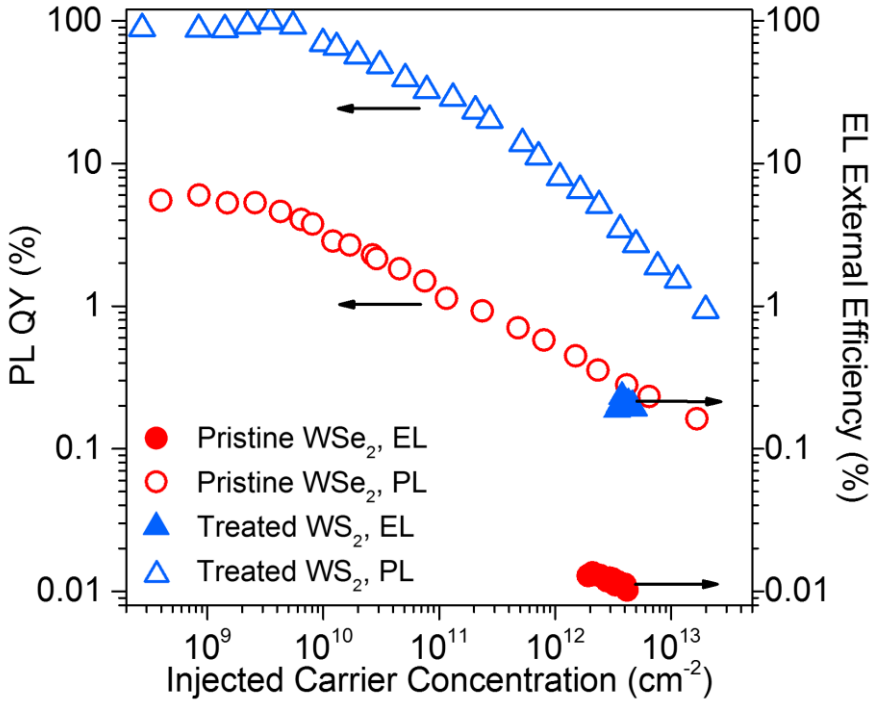

Supplementary Figure 14 | PL QY and EL external efficiency. PL QY and EL external efficiency as a function of injected carrier concentration measured for a WSe_2 device and a superacid-treated WS_2 device.

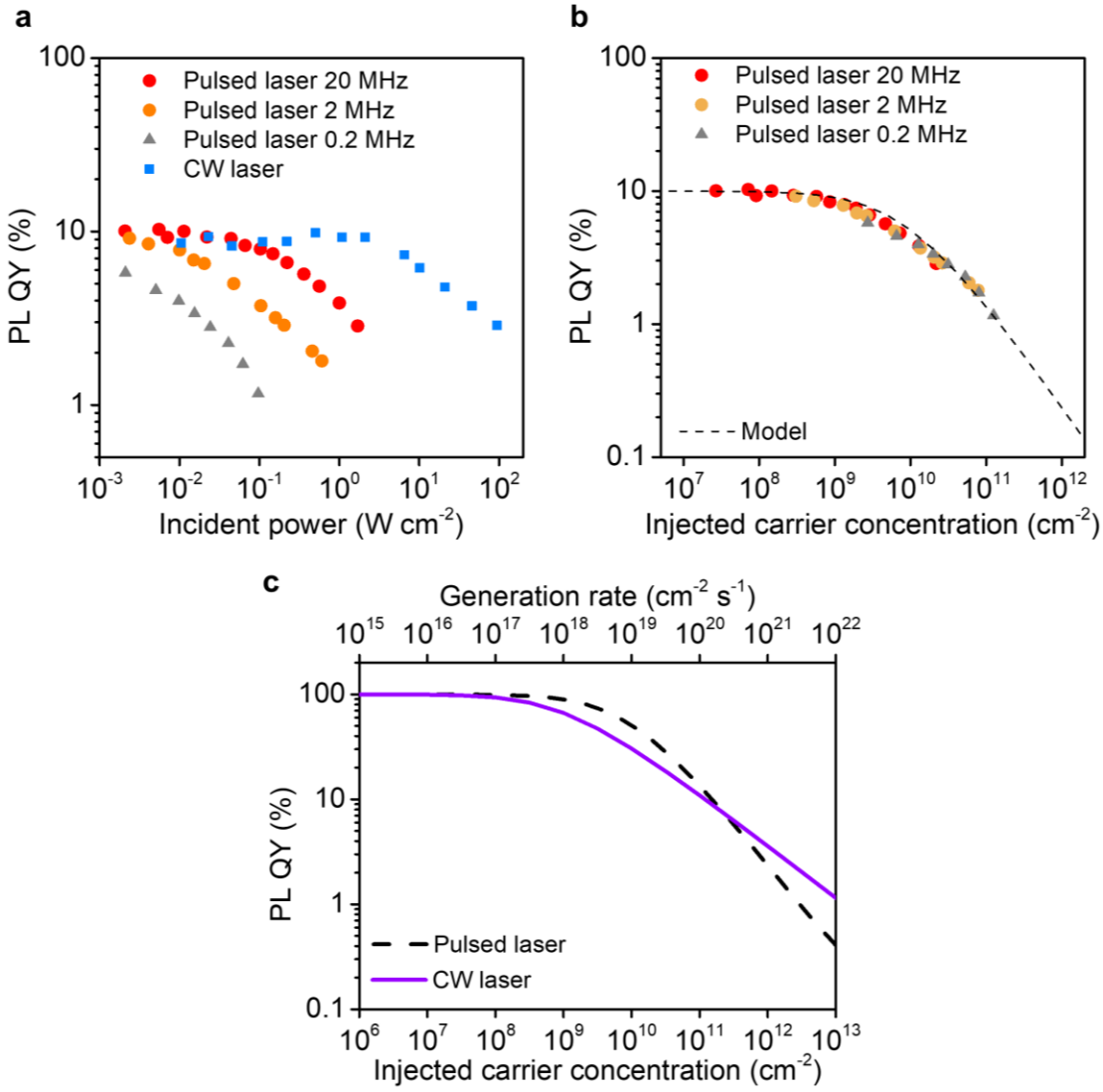

Supplementary Figure 15 | Quasi-steady-state PL QY. (a) QY measured as a function of incident average power for a CW laser and a pulsed laser with repetition rates of 0.2, 2, and 20 MHz; excitation wavelength is 514 nm in all cases. **(b)** Quasi-steady-state QY as a function of incident carrier concentration from measurements shown in panel **(a)**; dashed line shows recombination model. **(c)** Modeled recombination for steady state (purple) and quasi-steady-state (black) excitation.

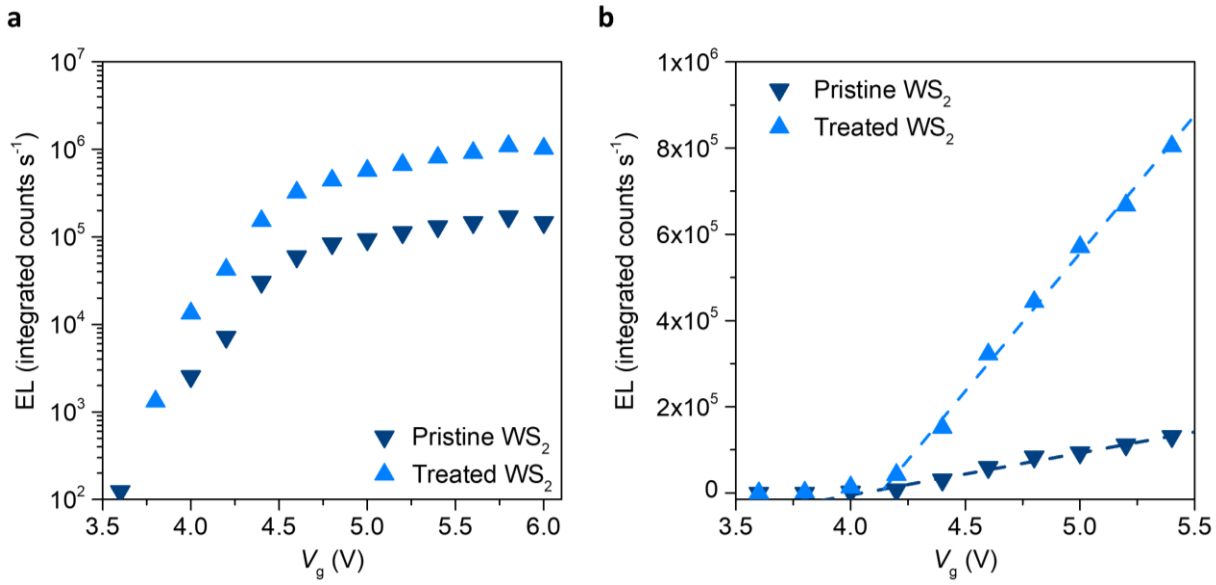

Supplementary Figure 16 | EL from WS_2 before and after superacid treatment. V_g dependence of EL from a WS_2 device before (pristine) and after superacid treatment (treated), plotted in **(a)** logarithmic and **(b)** linear scale.

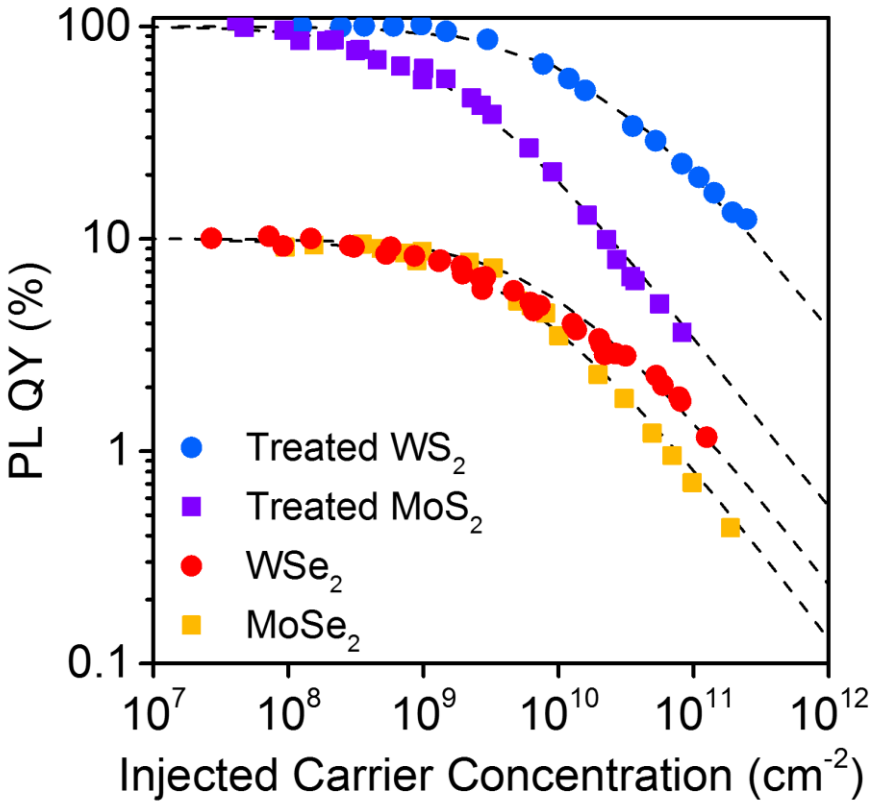

Supplementary Figure 17 | Quasi-steady state PL QY of TMDCs. PL QY of exfoliated $MoSe_2$, CVD WSe_2, and of superacid treated WS_2 and MoS_2 measured using a pulsed laser. Dashed lines show recombination model.

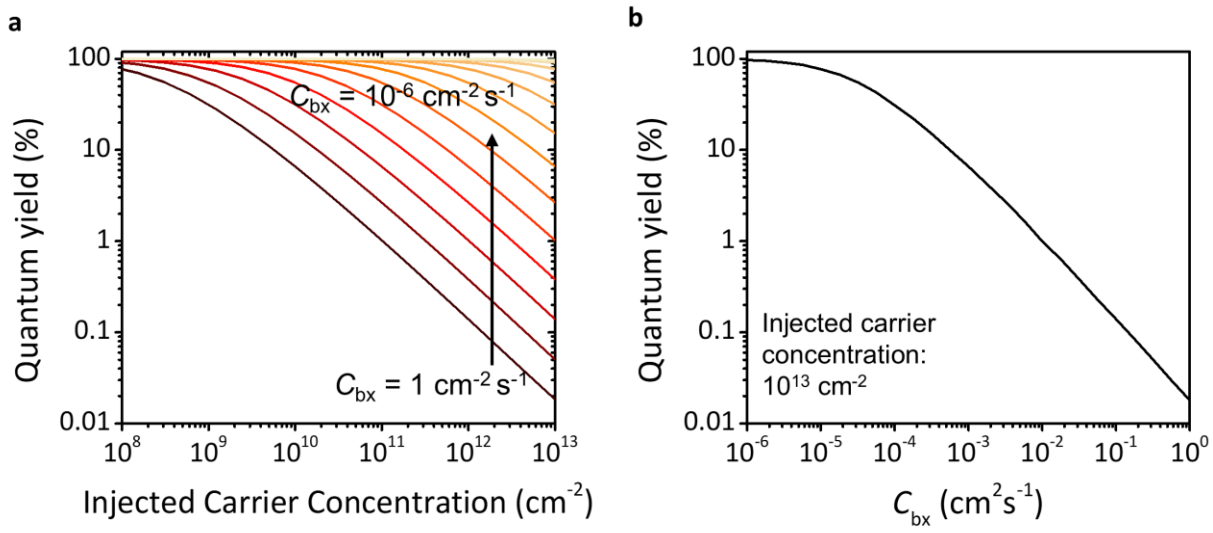

Supplementary Figure 18 | Estimation of PL QY for materials with varying C_{bx}. (a) An estimation of efficiency versus injected carrier concentration while tuning the C_{bx} of a material with a PL radiative lifetime of 10 ns. **(b)** The estimated QY of a material with varied C_{bx} from 1 to 10^{-6} cm^2s^{-1} under the injected carrier concentration of 10^{13} cm^{-2}.

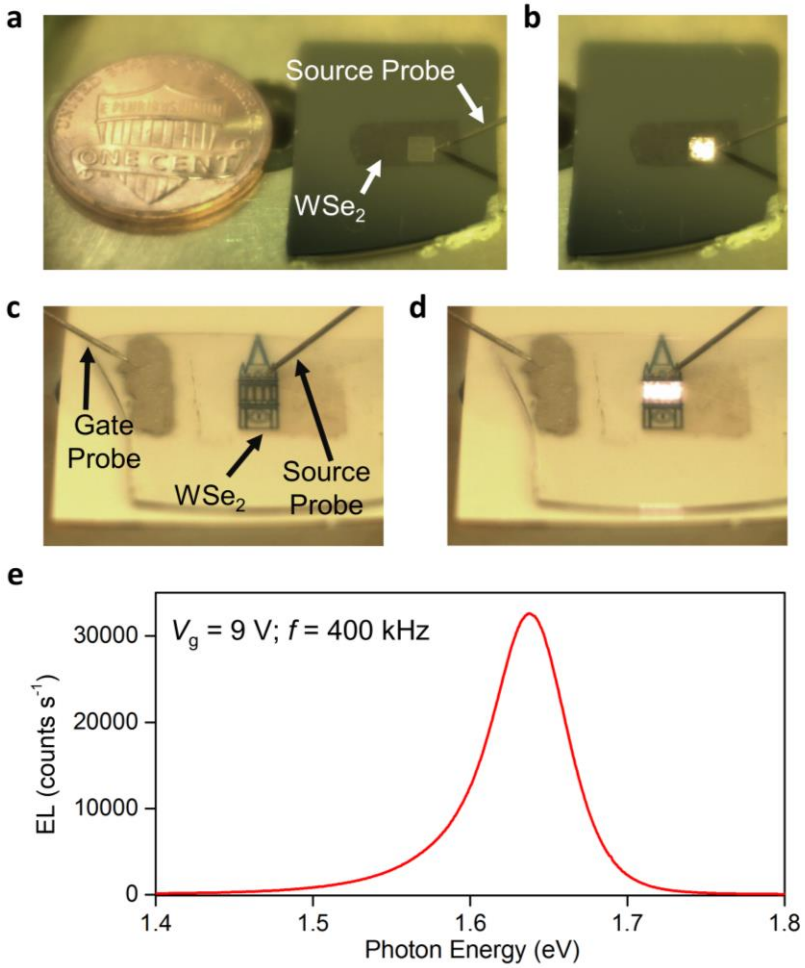

Supplementary Figure 19 | Millimeter-scale t-EL device. (a) Photograph of a WSe_2 t-EL device in the off-state taken in ambient room lights; a penny is shown as a size reference. The device grid structure is schematically shown in Fig. 4d. **(b)** Photograph of the same device in the on-state. **(c)** Photograph of a transparent WSe_2 t-EL device in the off-state, taken in ambient room lights. **(d)** Photograph of the same device in the on-state; note the emission at edges is due to light trapping within the quartz substrate. **(e)** EL spectra of device in panel **(b)** measured with a 10× objective (N.A. of 0.25); note that the device is larger than the objective field of view.

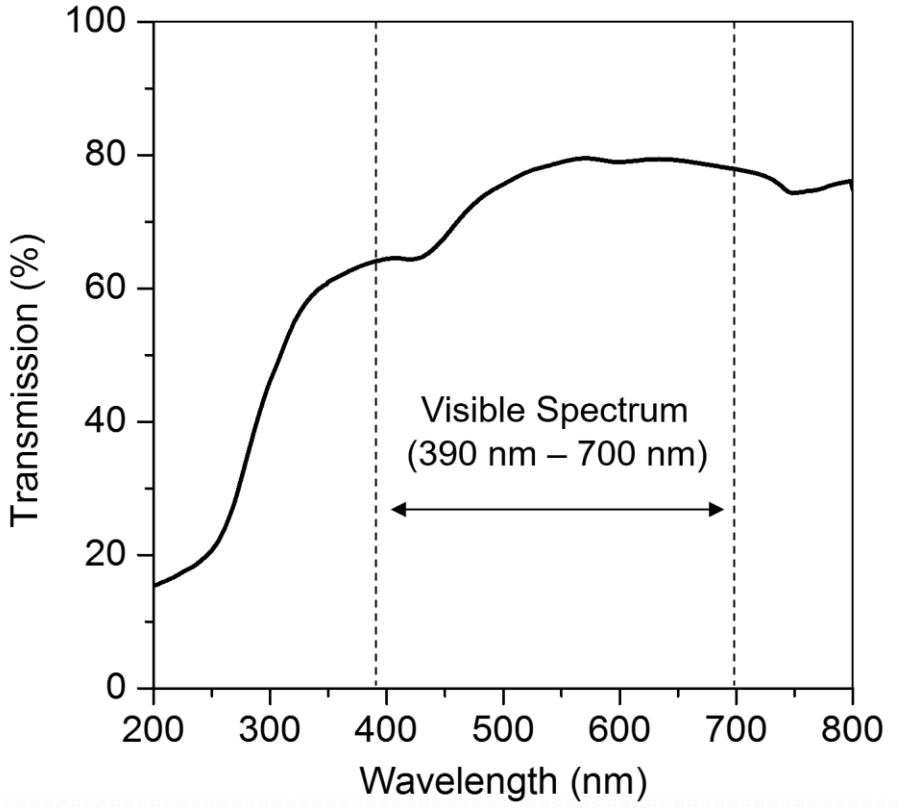

Supplementary Figure 20 | Transmittance of a millimeter-scale t-EL device. Transmission spectrum taken on the millimeter-scale WSe_2 device fabricated on fused quartz, using ITO/Al_2O_3 as the gate stack and ITO as the contact electrode.

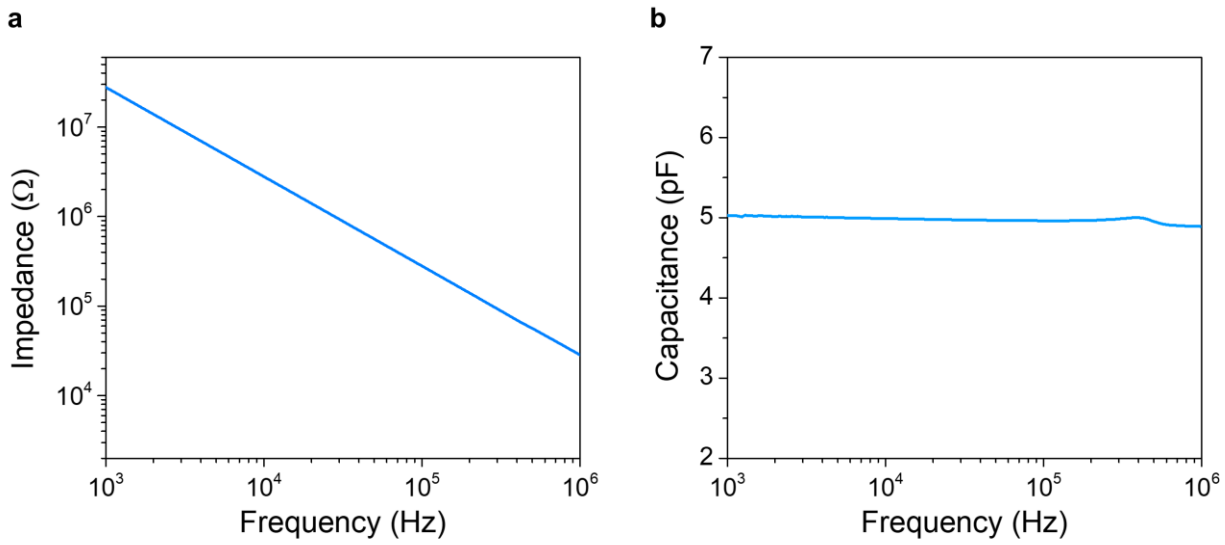

Supplementary Figure 21 | Gate oxide characterization. (a) Measured impedance versus frequency for a WSe_2 device with a 120 μm × 120 μm pad area fabricated on a 50 nm SiO_2/Si substrate. **(b)** Measured capacitance versus frequency for the same device shown in panel **(a)**.

Supplementary Notes

Supplementary Note 1. Quasi-steady state recombination kinetics.

The time dependent luminescence decay in 2D materials can be calculated using a recombination model for 2D excitonic systems presented in our previous work:

$$\frac{d\langle N(t)\rangle}{dt} = -\frac{\langle N(t)\rangle}{\tau_r} - C_{bx}\langle N(t)\rangle^2 \quad (1)$$

where $\langle N(t)\rangle$ is the exciton concentration as a function of time (t), τ_r is the exciton lifetime, and C_{bx} is the biexcitonic recombination rate[3-5]. Solving this differential equation yields:

$$\langle N(t)\rangle = \frac{\langle N(0)\rangle\, e^{-\frac{t}{\tau_r}}}{1 + \tau_r \langle N(0)\rangle C_{bx} (1 - e^{-\frac{t}{\tau_r}})} \quad (2)$$

where the boundary condition, $\langle N(0)\rangle$, is the initial exciton concentration. From Supplementary Equation 2, we can then calculate the PL QY during quasi-steady-state operation as a function of initial exciton density. The modeled values are in excellent agreement with quasi-steady-state QY measured using a pulsed laser with varying repetition rates as shown in Supplementary Fig. 15.

Supplementary Note 2. AC frequency dependence.

EL spectra measured with f ranging from 100 kHz to 10 MHz are shown in Supplementary Fig. 3a and the spectral shape was observed to be f independent (Supplementary Fig. 3b). The EL intensity per cycle shows minimal frequency dependence because $1/f$ is much larger than the EL decay time constant (~ 8 ns, Supplementary Fig. 2). This shows that the device can be operated at frequencies as high as 10 MHz, and is ultimately limited to a modulation frequency of 125 MHz corresponding to the EL decay time constant. This is the fastest electrically modulated light emitting device reported for TMDCs[6].

Supplementary Note 3. Current components during AC transient.

The total gate current ($I_{g,total}$) in a two-terminal t-EL device can be described by Supplementary Equation 3:

$$I_{g,total} = I_{g,DC} + I_{g,AC} \approx I_{g,AC} = I_{g,displacement} \quad (3)$$

where, $I_{g,DC}$ is the DC leakage current and $I_{g,AC}$ is the AC current at the gate electrode induced by the applied AC bias (V_g transients). From steady-state I_d-V_g measurements and capacitance measurements of the gate impedance as a function of frequency, we observe that the gate oxide shows no leakage current. Thus, the total gate current is mainly composed of the AC current, which is the displacement current generated by the changing electric fields in the device during a V_g transient. The corresponding current at the source terminal can be described by Supplementary Equation 4.

$$I_{s,total} = I_{s,DC} + I_{s,AC} \approx I_{s,AC} \quad (4)$$

The DC component of the current is again negligible. The AC current at the source contact is a combination of the electron, hole and displacement currents as shown in Supplementary Equation 5.

$$I_{s,AC} = I_{s,hole} + I_{s,electron} + I_{s,displacement} \quad (5)$$

It is not possible to experimentally measure these components separately, however Sentaurus simulations can help us understand the current components in more detail. Simulations (Supplementary Fig. 7) indicate that the major current components at the source electrode are the electron and hole currents, and their relative magnitude depends on the particular edge in the V_g transient. The simultaneous presence of electrons and holes in the semiconductor leads to EL emission.

Supplementary Note 4. EL dependence on Schottky barrier heights.

For devices with varying Schottky barrier (φ_B) heights, the relative intensity of EL at each V_g transient also shows large variations, although the integrated EL per cycle remains independent of φ_B. This can be qualitatively explained considering the specific example where we have hole selective; contacts to the semiconductor. In this case, during a $-V_g$ to $+V_g$ transient, the level of electrons which tunnel into the semiconductor is very low because of the large Schottky barrier height to electrons. This results in a smaller net bipolar carrier concentration in the semiconductor which translates to lesser EL. However, during the $+V_g$ to $-V_g$ transient, a large number of holes are injected into the semiconductor because of the smaller barrier height, resulting in a net larger bipolar carrier concentration, and hence larger EL. For the case of n-type contacts to the semiconductor, the mechanism can be similarly explained, and we obtain larger EL during the $-V_g$ to $+V_g$ transient relative to the $+V_g$ to $-V_g$ transient.

Supplementary Note 5. Gate oxide characterization.

To verify the gate oxide quality as well as to directly measure C_{ox}, capacitance vs. frequency measurements were performed on devices fabricated on 50 nm SiO_2/Si substrates as shown in Supplementary Fig. 21 over a frequency range of 1 kHz to 1 MHz. The measured capacitance of 5.1 pF is consistent with the calculated value of 6.91 pF. Furthermore, the measured impedance vs. frequency is in excellent agreement with the expected impedance of a direct capacitor (which is given as $X_c = (2\pi f C_{ox})^{-1}$, where X_c is the reactance of the gate capacitor). Furthermore, from DC measurements the leakage currents are below the noise level (pA range) of the measurement setup, and indicate that the device has a purely reactive impedance.

Supplementary Note 6. Efficiency calculation.

The EL internal efficiency of the t-EL device can be extracted from the ratio of the total number of emitted photons per cycle to the steady-state electron (n_0) and hole (p_0) concentrations:

$$\eta_{\mathrm{i}} = \frac{\int_0^T \int_0^L R\, dx\, dt}{(n_{\mathrm{o}} + p_{\mathrm{o}})L} = \beta(\mathrm{PL\ QY}) \tag{6}$$

Here T is the time period, L is the length of the device, R is the radiative recombination rate and β is the fraction of steady-state carriers which undergo recombination during a V_g transient. The value of (n_0+p_0) can be calculated using Supplementary Equation 6. During a -V_g to +V_g transient (total change of 2V_g), the net voltage dropped at the Schottky source contact is equal to the sum of the barrier heights to electrons and holes ($\varphi_{Bn} + \varphi_{Bp} = E_g$). Thus,

$$(n_{\mathrm{o}} + p_{\mathrm{o}}) = \frac{C_{\mathrm{ox}}\left[2V_{\mathrm{g}} - \left(\varphi_{\mathrm{Bn}} + \varphi_{\mathrm{Bp}}\right) q^{-1}\right]}{q} \tag{7}$$

To achieve steady-state carrier densities, sufficient voltage must be applied to enable large band bending and thus achieve significant tunneling through the Schottky barriers. As such this equation is only valid for sufficiently high V_g, which is shown in Supplementary Fig. 13. The integral in the numerator is equal to the total number of photons emitted per cycle. The internal efficiency is unity when the PL QY is 100% and all of the steady-state carriers undergo recombination (β = 1). Practically, due to the finite slew rate of the AC source and a finite radiative recombination rate, a fraction of the steady-state carriers exit the semiconductor through the source contact without recombining ($\beta \neq 1$). The external efficiency is given by:

$$\eta_{\mathrm{e}} = \eta_{\mathrm{i}}\, \eta_{\mathrm{ext}} \tag{8}$$

where η_{ext} is the light extraction efficiency. This is calculated using $(4n^2)^{-1}$ where n is the refractive index of the medium, as well as the optical interference from the Si substrate with a 50 nm SiO_2 layer. The enhancement factor for Si/SiO_2 is experimentally determined to enhance the light-outcoupling by 1.6× for WSe_2 and 2× for WS_2.

Supplementary Methods

Three independent approaches were used to verify the system calibration, and are discussed in detail in our previous work.[3] In the first approach, the wavelength of the spectrometer was calibrated using Ar and Kr lamps (Newport) as reference. The instrument function versus wavelength of the system was obtained by measuring the response of a Lambertian light source generated under the objective through the illumination from a temperature-stabilized lamp (ThorLabs SLS201) onto a diffuse reflector surface. The system efficiency was calibrated by measuring the response of the 514 nm laser focused on the diffuse reflector. In the second approach, we cross-calibrated using a silicon photodiode which was able to acquire a fraction of the PL but is independent of the optical path of objective. In the third approach, the calibrations were performed using a sample with a known QY close to 100% (Rhodamine 6G in methanol). These three approaches were in good agreement with each other (<15% error).

Supplementary References

1. Chuang, S. *et. al.* MoS_2 p-type transistors and diodes enabled by high workfunction MoO_x contacts. *Nano Lett.* **14**, 1337-1342 (2014)
2. Ramasubramaniam, A. Large excitonic effects in monolayers of molybdenum and tungsten dichalcogenides. *Phys. Rev. B* **86**, 115409 (2012).
3. Amani, M. *et. al*. Near-unity photoluminescence quantum yield in MoS_2. *Science* **350**, 1065-1068 (2015).
4. Amani, M. *et. al*. Recombination kinetics and effects of superacid treatment in sulfur- and selenium-based transition metal dichalcogenides. *Nano Lett.* **16**, 2786-2791 (2016).
5. Kim, H., Lien, D.-H., Amani, M., Ager, J. W. & Javey, A. Highly stable near-unity photoluminescence yield in monolayer MoS_2 by fluoropolymer encapsulation and superacid treatment. *ACS Nano* **11**, 5179-5185 (2017).
6. Liu, C.-H. *et. al.* Nanocavity integrated van der Walls heterostructure light-emitting tunneling diode. *Nano Lett.* **17**, 200-205 (2017).